Preferential enhancement of convective heat transfer over drag via near-wall turbulence manipulation using spanwise wall oscillations

Lou Guérin, Cédric Flageul, Laurent Cordier, Stéphane Grieu, Lionel Agostini

▶ **To cite this version:**

Lou Guérin, Cédric Flageul, Laurent Cordier, Stéphane Grieu, Lionel Agostini. Preferential enhancement of convective heat transfer over drag via near-wall turbulence manipulation using spanwise wall oscillations. International Journal of Heat and Fluid Flow, 2024, 110, pp.109564. 10.1016/j.ijheatfluidflow.2024.109564 . hal-04357505

HAL Id: hal-04357505
https://hal.science/hal-04357505v1

Submitted on 13 Sep 2024

HAL is a multi-disciplinary open access archive for the deposit and dissemination of scientific research documents, whether they are published or not. The documents may come from teaching and research institutions in France or abroad, or from public or private research centers.

L'archive ouverte pluridisciplinaire **HAL**, est destinée au dépôt et à la diffusion de documents scientifiques de niveau recherche, publiés ou non, émanant des établissements d'enseignement et de recherche français ou étrangers, des laboratoires publics ou privés.

Distributed under a Creative Commons Attribution 4.0 International License

International Journal of Heat and Fluid Flow 110 (2024) 109564

Contents lists available at ScienceDirect

International Journal of Heat and Fluid Flow

journal homepage: www.elsevier.com/locate/ijhff

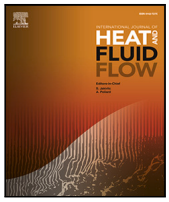

Preferential enhancement of convective heat transfer over drag via near-wall turbulence manipulation using spanwise wall oscillations

Lou Guérin [a,*], Cédric Flageul [a], Laurent Cordier [a], Stéphane Grieu [b], Lionel Agostini [a]

[a] Pprime institute, Curiosity team, CNRS, Université de Poitiers, ISAE-ENSMA, Poitiers, France
[b] PROMES-CNRS (UPR 8521) University of Perpignan Via Domitia, Perpignan, France

ARTICLE INFO

Keywords:
Direct numerical simulation
Wall-bounded turbulent flow
Dissimilar heat transfer
Spanwise wall oscillations

ABSTRACT

This study investigates the manipulation of convective heat transfer through spanwise wall oscillations in a turbulent channel flow. Direct numerical simulations are performed at $Re_\tau = 180$ and $Pr = 1$.

The primary focus of this work is to explore the heat transfer response to oscillation parameters that promote drag increase, a regime that has received limited attention. By adopting an extended oscillation period ($T^+ = 500$) and amplitude ($W^+ = 30$), which have been reported to enhance drag, a remarkable dissimilarity between momentum and heat transport emerges. Under these conditions, the convective heat transfer undergoes a substantial 15% intensification, while the drag increases by a comparatively moderate 7.7%, effectively breaking the Reynolds analogy. To elucidate the physical mechanisms responsible for this dissimilar behaviour, a comprehensive statistical analysis is conducted. The control effect on the near-wall streaks and the associated mixing of momentum and heat is investigated by examining the energy distribution across scales and wall-normal locations. This analysis provides valuable insights into the control's impact on the turbulent structures. Furthermore, the correlation between wall-normal velocity fluctuations and both streamwise velocity and temperature fluctuations is scrutinized to understand the modification of sweep and ejection events, which drive the transport of momentum and heat. The Fukagata–Iwamoto–Kasagi (FIK) identity is employed to identify the contributing factors to the changes in drag and heat transfer. The analysis highlights the importance of the pressure term in the streamwise velocity equation and the linearity of the temperature equation. Further investigation is necessary to fully unravel the complex mechanisms governing the decoupling of heat and momentum transport. The results of this study underscore the potential of using unconventional spanwise wall oscillations parameters to preferentially enhance convective heat transfer while minimizing the associated drag penalty.

1. Introduction

Turbulent flows play an important role in determining the performance characteristics of a wide range of industrial equipment and environmental applications. One significant consequence of turbulence is the increased mixing of momentum, leading to high friction drag on surfaces, which intensifies as the Reynolds number increases. Friction drag can significantly affect the efficiency and effectiveness of a device or process in a broad range of applications (Ricco et al., 2021). This is particularly relevant in the transport sector, encompassing both self-propelling bodies moving through fluids and fluids being transported via ducts or pipes for example (Abdulbari et al., 2013). Due to global warming issues, there is an increasing pressure to reduce transport-related emissions, with friction drag being a significant contributor to these emissions (Asidin et al., 2019). On the other hand, improving heat exchanger performance is a primary technological challenge for a wide range of engineering systems that involve cooling or heating processes. The goal is to achieve greater efficiency, in line with the industrial and societal imperatives for cost-effective and sustainable energy transfer. Enhancing the turbulent fluxes within the wall-bounded region is generally beneficial for improving heat transfer (Zhang et al., 2020). Therefore, a balance needs to be found between drag-induced losses and heat transfer.

Controlling the boundary layer to decrease drag has been an active area of research for many years. In this regard, imposing spanwise wall oscillations (SWO) has emerged as a promising technique as extensively reviewed by Ricco et al. (2021). While a significant portion of the work in this field has focused on identifying optimal control strategies by determining the most effective control parameters and evaluating the actual energy savings (considering the energy required for applying the control), few studies have thoroughly investigated the underlying

* Correspondence to: 2 Bd des Frères Lumière, 86360 Chasseneuil-du-Poitou, France.
E-mail address: lou.guerin@univ-poitiers.fr (L. Guérin).

https://doi.org/10.1016/j.ijheatfluidflow.2024.109564
Received 22 May 2024; Received in revised form 16 August 2024; Accepted 4 September 2024
0142-727X/© 2024 The Author(s). Published by Elsevier Inc. This is an open access article under the CC BY license (http://creativecommons.org/licenses/by/4.0/).

mechanisms driving drag reduction. The exact mechanisms remain not fully understood. Simulations and experiments have consistently demonstrated the potential of SWO to lead substantial drag reductions, with values around 40%–50% observed at low Reynolds numbers (Touber and Leschziner, 2012; Viotti et al., 2014). The oscillating wall motion introduces a time-varying spanwise strain near the wall, known as the Stokes layer, which disrupts the formation of streaks, weakens quasi-streamwise vortices, and thickens the viscous sublayer (Agostini et al., 2014b; Quadrio and Ricco, 2004; Choi and Clayton, 2001). These modifications to the near-wall turbulence dynamics lead to reduced momentum mixing and, consequently, lower shear stress at the wall. The efficacy of drag reduction is contingent upon various SWO parameters, such as the oscillation amplitude, frequency, and waveform. Upon the onset of SWO, a transient phase lasting 2–3 oscillation periods occurs, ultimately landing in the attainment of the minimum drag state. Once this low-drag state is reached, phase variations synchronized with the wall oscillation period can be observed, with the drag undergoing a strengthening and weakening phase twice during each actuation cycle.

Numerous studies have aimed to identify the optimal set of parameters for maximizing drag reduction (Gatti and Quadrio, 2013). Letting u_τ and ν denote the friction velocity and kinematic viscosity, respectively, prior investigations (Ricco et al., 2021; Quadrio and Ricco, 2004) have determined that the optimal oscillation period for achieving maximum drag reduction, is approximately $T^+ = 100$, where $T^+ = \frac{Tu_\tau^2}{\nu}$ is the dimensionless oscillation period. The optimal period exhibits relative robustness across different Reynolds numbers, with comparable values observed in turbulent channel flows up to $\mathrm{Re}_\tau = 6000$ (Marusic et al., 2021), where $\mathrm{Re}_\tau = \frac{Hu_\tau}{\nu}$ and H represents the channel half-height. A parametric study conducted by Quadrio and Ricco (2004) using Direct Numerical Simulations (DNS) at $\mathrm{Re}_\tau = 200$ demonstrated a maximum drag reduction of 44.7% with an oscillation period $T^+ = 100$ and amplitude $W^+ = \frac{W}{u_\tau} = 27$. It is noteworthy that within the range of oscillation parameters investigated ($0 \leq W^+ \leq 30$, $0 \leq T^+ \leq 300$), an overall drag increase was not observed. To the best of the authors' knowledge, the only documented instance of a net drag increase at low Reynolds numbers is reported in the simulations of Jung et al. (1992), specifically for an extended oscillation period of $T^+ = 500$ with $W = 0.8Q_x$, where Q_x denotes the fixed streamwise flow rate, at $\mathrm{Re}_\tau = 200$. This higher period value was found to induce significantly more pronounced variations in the periodic equilibrium drag compared to shorter periods.

While numerous studies have been conducted to determine the forcing parameters that optimally reduce turbulent drag, few have analysed the effects on heat transfer. As momentum and heat transport are intrinsically connected through the Reynolds analogy, the effect of oscillations on drag should be mirrored in the heat transfer response. The study of the heat transfer response to oscillatory wall forcing is then of primary importance. Fang et al. (2009) performed Large Eddy Simulations (LES) at $\mathrm{Re}_\tau = 180$ and $\mathrm{Pr} = 0.72$ on a weakly compressible flow at Mach = 0.5, employing oscillation periods near the optimal value and varying the amplitude from $6.35 \leq W^+ \leq 19.05$. Their results demonstrated the consistency between temperature and streamwise velocity streaks, despite drastic changes induced by oscillations. Fang et al. (2010) later proved the consistency between momentum and heat transport, highlighting their high correlation with turbulent motions. Utilizing in-phase oscillations, Fang and Lu (2010) observed significant drag increase, primarily during the transient stage. For all investigated waveforms, heat transfer variations exhibited a striking resemblance to drag. Ni et al. (2016) extended these findings to higher Mach numbers (Mach = 2.9), introducing a corrected version of the wall-heat flux by subtracting the Stokes solution. This corrected wall-heat flux was shown to vary in a similar manner to the drag.

Decoupling heat and momentum transport to substantially increase heat transfer while limiting frictional penalties, often referred to as *dissimilar heat transfer* (Uchino et al., 2017), has garnered significant interest. Various control strategies have been implemented to achieve this objective (Yamamoto et al., 2013; Uchino et al., 2017; Kaithakkal et al., 2021). For instance, Yamamoto et al. (2013) achieved up to 24% drag reduction along with over 50% increase in heat transfer using wall blowing and suction control in turbulent channel flow at $\mathrm{Re}_\tau = 100,\ 150,$ and 300 with a passive scalar temperature field. This was attained even with the unfavourable unity Prandtl number and Uniform Heat Generation (UHG) thermal boundary conditions, which induce identical boundary conditions and source terms for streamwise velocity and temperature, hindering dissimilarity between drag and heat transfer. However, while wall blowing/suction has shown promising results, its practical implementation remains challenging at high Reynolds numbers. Uchino et al. (2017) investigated this dissimilarity at $\mathrm{Re}_\tau = 180$ through DNS by introducing streamwise travelling wave-like deformation. A Constant Temperature Difference (CTD) boundary condition was imposed on the channel walls and the temperature was considered as a passive scalar with $\mathrm{Pr} = 1$. To characterize the dissimilarity between the momentum and heat transfer, Uchino et al. (2017) introduced the analogy factor, defined as $A_n = \frac{\mathrm{St}/\mathrm{St}^0}{C_f/{C_f}^0}$, where St and St^0 are the actuated and unactuated Stanton numbers, and C_f and ${C_f}^0$ are the actuated and unactuated skin friction coefficients, respectively. To achieve a heat transfer increase exceeding that of drag, one would need to obtain A_n greater than unity and as large as possible while ensuring heat transfer enhancement ($\frac{\mathrm{St}}{\mathrm{St}^0} > 1$). A parametric study led to a time-averaged analogy factor of 1.13 for a large wall deformation amplitude and a short wall deformation period. The choice of thermal boundary conditions in a turbulent channel flow can significantly influence the potential for achieving dissimilar heat transfer through control, as demonstrated by Flageul et al. (2015). Kasagi et al. (2012) conducted a comparative analysis of different temperature boundary conditions, including Uniform Heat Generation (UHG), Constant Heat Flux (CHF), and Constant Temperature Difference (CTD), employing the FIK identities (Fukagata et al., 2002) and their heat transfer extension (Hasegawa and Kasagi, 2011). Their findings revealed that the optimal scenario for obtaining dissimilarity arises when CTD thermal boundary conditions are applied in conjunction with a Prandtl number far from unity. Conversely, the most challenging case for achieving dissimilarity occurs with UHG thermal boundary conditions and unity Prandtl number, as this combination induces analogous boundary conditions and source terms for both the streamwise velocity and temperature fields.

The studies by Rouhi et al. (2022), Kuwata (2022) have demonstrated that passive control methods can be used to create Kelvin–Helmholtz (K–H) rollers, which can weaken drag while strengthening heat transfer. These rollers play an important role in disrupting the Reynolds analogy. Indeed, by introducing inflection point in the wall-normal distribution of the streamwise velocity gradient, passive control devices initiate the formation of K–H rollers with a clockwise rotation in the near-wall region. The direction of rotation of these rollers has a significant impact on the variation of heat transfer and drag. For heat transfer, the mixing induced by the rollers is beneficial regardless of the direction of rotation, as it facilitates the transport of heat away from the wall, leading to improved heat-transfer rates. In contrast, the effect on drag is more complex. The clockwise rotation of the K–H rollers reduces the velocity gradient at the wall, weakening skin friction. The K–H rollers thus selectively reduce drag while enhancing heat transfer, underpinning the favourable breakdown of the Reynolds analogy. This insight highlights the critical role of flow structures, particularly K–H rollers, in achieving disparate improvements in heat transfer and drag. By manipulating these flow structures through passive methods, such as high-aspect-ratio longitudinal ribs, efficient heat transfer surfaces with minimal drag penalties can be achieved.

This study, performed by DNS at $\mathrm{Re}_\tau = 180$ and $\mathrm{Pr} = 1$, aims to investigate the effect of spanwise wall oscillations on achieving a dissimilar increase in convective heat transfer compared to drag. In Section 2, we describe the flow conditions and detail the numerical procedure. Validation of uncontrolled numerical simulations is carried out in Section 3 by comparing the obtained DNS statistics with

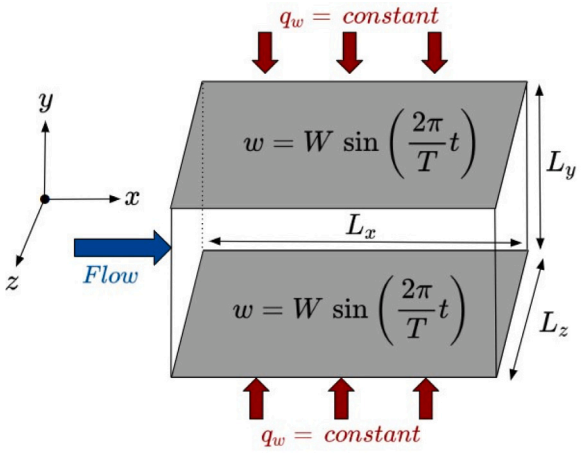

Fig. 1. Schematic of the flow configuration.

references at $\mathrm{Re}_\tau = 180$ and analysing the influence of mesh sizes. Section 4 introduces and validates the control strategy. The results, presented in Section 5, initially focus on identifying parameters outside the range studied in Quadrio and Ricco (2004) that enable a heat transfer increase. The parameters $T^+ = 500$ and $W^+ = 30$ serve as the starting point for investigation, as this period has been shown in Jung et al. (1992) to cause an overall drag increase. The FIK identity decompositions (Fukagata et al., 2002) are then investigated to identify the different components contributing to heat transfer and drag variations. Structural analysis of the streaks and quadrant analysis are then performed to gain a better understanding of the thermal/momentum enhancements. While the main objectives of this work are to validate the configuration and extend spanwise wall oscillations to control the relative increase of convective heat transfer over drag, determining optimal parameters for maximizing this disproportionality is beyond the scope of the present study. Instead, the focus is set on fundamentally characterizing the mechanisms responsible for the greater increase in heat transfer compared to drag, induced by the oscillatory wall forcing. To the best of the authors' knowledge, this study represents the first instance of thermal transport enhancement exceeding the friction increase using spanwise wall oscillations in an incompressible flow, effectively breaking the Reynolds analogy.

2. Flow conditions and numerical procedure

Direct numerical simulations of a canonical channel flow are performed at $\mathrm{Re}_\tau \approx 180$ in a domain defined as:

$$\Omega = \left\{ \boldsymbol{x} = \left(x\ y\ z\right)^\intercal \in \mathbb{R}^3 \mid x \in [0, L_x],\ y \in [0, L_y],\ z \in [0, L_z] \right\},$$

with x, y, z representing the streamwise, wall normal, and spanwise components, respectively (see Fig. 1). The velocity, pressure and temperature fields are given by $\boldsymbol{u}(\boldsymbol{x},t) = \left(u(\boldsymbol{x},t)\ v(\boldsymbol{x},t)\ w(\boldsymbol{x},t)\right)^\intercal$, $p(\boldsymbol{x},t)$ and $T(\boldsymbol{x},t)$.

2.1. Physical modelling

The evolution of the velocity $\boldsymbol{u}$ is given by the incompressible Navier–Stokes equations, and that of the temperature T corresponds to the passive transport of a scalar by the velocity $\boldsymbol{u}$. In most applications, significant heat transfer leads to buoyancy forces which would result in an active scalar temperature. In this study, these forces are neglected in order to simplify the analysis. Assuming a flow density equal to 1, the following set of governing equations is obtained:

$$\begin{cases} \nabla \cdot \boldsymbol{u} = 0 \\ \dfrac{\partial \boldsymbol{u}}{\partial t} + (\boldsymbol{u} \cdot \nabla)\,\boldsymbol{u} = -\nabla p + \nu \Delta \boldsymbol{u} \\ \dfrac{\partial T}{\partial t} + \boldsymbol{u} \cdot \nabla T = \alpha \Delta T, \end{cases} \tag{1}$$

where α is the thermal conductivity. Hereafter, bulk quantities are defined for any field χ as $\chi_b = \frac{1}{|\Omega|}\int_\Omega \langle \chi \rangle_t \, \mathrm{d}\Omega$, where $|\Omega|$ is the fluid inner volume of the channel and $\langle\cdot\rangle_t$ the time average. By extension, $\langle\cdot\rangle_{x,z,t}$ denotes the average over time and the directions x and z. The flow rate U_b is therefore obtained for $\chi = u$ and the bulk temperature T_b for $\chi = T$.

In numerical simulations, periodic boundary conditions are imposed in the streamwise and spanwise directions of the flow, as well as homogeneous Dirichlet boundary conditions on the walls for both velocity and temperature (see below). By definition, χ_w represents the boundary conditions imposed on any variable χ on the walls, i.e. $\chi_\mathrm{w} = \left\{ \chi(\boldsymbol{x}) \mid x \in [0, L_x],\ z \in [0, L_z] \text{ and } y = 0 \text{ or } y = L_y = 2H \right\}$.

Concerning the thermal boundary condition, several options are available. Here, a Mixed Boundary Condition (MBC) is imposed, see Kasagi et al. (1992) for a more complete presentation. When MBC boundary conditions are specified, an averaged constant uniform heat flux q_w is applied on the walls (see Fig. 1) while assuming that the temperature fluctuations at the wall are null. Therefore, the temperature at the walls is not time-dependent ($T_\mathrm{w} = \langle T_\mathrm{w} \rangle_t$). Using the global heat balance for constant heat flux, it can be shown that $\langle T_\mathrm{w} \rangle_t$ increases linearly in the streamwise direction ($\langle T_\mathrm{w} \rangle_t = Ax + T_0$), as stated in Kasagi et al. (1992). For this type of thermal boundary condition, an appropriate non-dimensional form of the temperature is defined as:

$$\Theta = \frac{T - \langle T_\mathrm{w} \rangle_t}{T_b - \langle T_\mathrm{w} \rangle_t}. \tag{2}$$

It can also be shown that the scaling temperature $\langle T_\mathrm{w} \rangle_t - T_b$ is constant by applying Newton's law of cooling, $q_w = h(\langle T_\mathrm{w} \rangle_t - T_b)$ where the heat transfer coefficient h is constant, and using the constant flux assumption. Furthermore, the assumption of zero fluctuations at the wall can be directly incorporated in the prescription of the boundary condition:

$$\Theta_\mathrm{w} = \Theta(T = T_\mathrm{w}) = \frac{T_\mathrm{w} - \langle T_\mathrm{w} \rangle_t}{T_b - \langle T_\mathrm{w} \rangle_t} = \frac{T'_\mathrm{w}}{T_b - \langle T_\mathrm{w} \rangle_t} = 0. \tag{3}$$

Finally, the bulk temperature is constant ($\Theta_b = \Theta(T = T_b) = 1$) ensuring the thermal stationary condition.

The Mixed Boundary Conditions exhibit a similar analogy (in between streamwise velocity and temperature) to UHG, albeit with a different source term for temperature, and benefit from extensive documentation with numerous available databases on the unactuated case at various Reynolds numbers (Abe et al., 2009; Seki et al., 2006). Moreover, the present work establishes that the source term difference does not significantly contribute to the achieved dissimilarity, rendering MBC analogous to UHG for this specific purpose. The relevance of working with such a configuration, characterized by initial similarities between temperature and streamwise velocity, lies in its ability to limit the potential factors of initial dissimilarity, thereby simplifying the subsequent analysis of dissimilar heat transfer. Consequently, the current study employs a passive scalar temperature with MBC and unity Prandtl number to facilitate a focused investigation of the dissimilarity mechanisms.

2.2. Non-dimensionalization

The dimensionless Navier–Stokes equations are defined as:

$$\begin{cases} \nabla^\star \cdot \boldsymbol{u}^\star = 0 \\ \dfrac{\partial \boldsymbol{u}^\star}{\partial t^\star} + \left(\boldsymbol{u}^\star \cdot \nabla^\star\right)\boldsymbol{u}^\star = -\nabla^\star p^\star + \dfrac{1}{\mathrm{Re}} \Delta^\star \boldsymbol{u}^\star + \boldsymbol{f}^\star \\ \dfrac{\partial \Theta}{\partial t^\star} + \boldsymbol{u}^\star \cdot \nabla^\star \Theta + A^\star u^\star = \dfrac{1}{\mathrm{Pe}} \Delta^\star \Theta \end{cases} \tag{4}$$

with

$$\Theta = \frac{T - \langle T_w \rangle_t}{T_b - \langle T_w \rangle_t},\ \boldsymbol{x}^\star = \frac{\boldsymbol{x}}{H},\ t^\star = t\frac{U_b}{H},\ p^\star = \frac{p}{U_b^2},\ \boldsymbol{u}^\star = \frac{\boldsymbol{u}}{U_b},\ A^\star = A\frac{H}{T_b - \langle T_w \rangle_t}.$$

Introducing the variable Θ given by Eq. (2) into the temperature equation generates a forcing term $f_\Theta = Au$. The approach to implement this forcing term follows the constant bulk temperature (CBT) method, wherein $\Theta_b = 1$ is mandated at each iteration. For velocity, a constant flow rate (CFR) strategy is imposed, fixing $U_b = \frac{2}{3}$ at each iteration. The corresponding forcing term $\boldsymbol{f}^\star = \begin{pmatrix} f_x^\star & 0 & 0 \end{pmatrix}^\intercal$ arises from the mean pressure gradient driving the flow. This compensates for viscous friction to achieve steady state. The CFR procedure is common and will not be detailed here. It is worth mentioning that the source term f_Θ has u as a factor and therefore, contrary to the forcing term in the UHG case, is not uniform in space, which differs from the forcing term $f_x^\star$.

Subsequently, for simplicity, notations without superscript $\cdot^\star$ will refer to dimensionless values. Notations with superscript $\cdot^+$ will denote values scaled by wall units, i.e. non-dimensionalized by u_τ, $\Theta_\tau = \frac{\alpha}{u_\tau}\frac{\partial \langle \Theta_w \rangle_{x,z,t}}{\partial y}$ and Re_τ, the friction velocity, friction temperature and friction Reynolds number, respectively.

The two key dimensionless numbers characterizing the flow are the Reynolds number $\mathrm{Re} = \frac{U_b H}{\nu}$ and the Péclet number $\mathrm{Pe} = \mathrm{Re} \times \mathrm{Pr}$, where Pr is the Prandtl number defined as $\mathrm{Pr} = \frac{\nu}{\alpha}$. For this study, the Prandtl number is set to $\mathrm{Pr} = 1$ to obtain higher similarity between the velocity and temperature equations as $\mathrm{Pe} = \mathrm{Re}$. In this case, identical boundary conditions are utilized for both velocity and temperature. This enables simpler analysis, as differences in the variations of drag and heat transfer induced by actuation will not originate from disparities in the unactuated boundary conditions or Prandtl number effects. This channel flow configuration was selected for its simplicity and ability to induce substantial similarity between the streamwise velocity and temperature fields.

In this configuration, the sole differences between the streamwise velocity and temperature fields that could potentially facilitate attaining dissimilar heat transfer are:

- The source term difference, f_x is uniform in space while f_Θ is not.
- The pressure term in the streamwise velocity equation which indirectly applies the divergence-free condition of the continuity equation. This term is absent in the temperature equation.
- The linearity of the convective term in the temperature equation does not apply to streamwise velocity.

The friction coefficient, C_f, and Nusselt number, Nu, characterize drag and heat transfer, respectively. In the current configuration, these quantities are defined by the following equations:

$$C_f(t) = \frac{\tau_w}{\frac{1}{2}\rho U_b^2} = \frac{2\nu}{U_b^2}\frac{\partial \langle u \rangle_{x,z}}{\partial y}_{\mathrm{w}} = \frac{9\nu}{2}\frac{\partial \langle u \rangle_{x,z}}{\partial y}_{\mathrm{w}}, \tag{5}$$

$$\mathrm{Nu}(t) = \frac{2Hh}{\lambda} = \frac{2}{T_b - T_w}\frac{\partial \langle T \rangle_{x,z}}{\partial y}_{\mathrm{w}} = 2\frac{\partial \langle \Theta \rangle_{x,z}}{\partial y}_{\mathrm{w}}. \tag{6}$$

where h is the convective heat transfer coefficient and λ is the thermal conductivity. The first equation simplifies by injecting the shear stress $\tau_w = \mu\frac{\partial \langle u \rangle_{x,z}}{\partial y}_{\mathrm{w}}$ and the imposed bulk velocity $U_b = \frac{2}{3}$. The Nusselt number definition uses the full height of the channel $2H$ as a reference length. Its simplification arises from Newton's law of cooling for internal flows $h = \frac{q_w}{T_w - T_b}$, with $q_w = -\lambda\frac{\partial \langle T \rangle_{x,z}}{\partial y}_{\mathrm{w}}$ and the above non-dimensionalization of H and Θ. Computation of both dimensionless parameters utilizes the forcing terms, f_x and f_Θ.

2.3. Fluctuating quantities

For validation, current simulations are compared to reference uncontrolled cases (see Section 3). Correspondence between simulations and canonical cases provides a measure of implemented model and numerical method veracity.

To enable forthcoming validations, the definition of the time-wise and phase-wise averages must be clearly established. Any general field variable χ, in the unactuated case, representing velocity components, temperature or pressure can be decomposed as

$$\chi(x, y, z, t) = \overline{\chi}(y) + \chi'(x, y, z, t), \tag{7}$$

where $\overline{\chi} = \langle \chi \rangle_{x,z,t}$ is the time and space average at a particular wall-normal location y, and χ' are the stochastic fluctuations in absence of wall oscillations.

For the actuated field, the stochastic fluctuations are noted as χ'' and are obtained by removing the phase average of the raw field:

$$\chi''(x, y, z, t) = \chi(x, y, z, t) - \widetilde{\chi}(\epsilon, y), \tag{8}$$

with the phase average $\widetilde{\chi}(\epsilon, y)$ defined as:

$$\widetilde{\chi}(\epsilon, y) = \frac{1}{N}\sum_{n=1}^{N} \langle \chi(x, y, z, \epsilon + nT) \rangle_{x,z}, \tag{9}$$

and where $\epsilon \in [0, T]$ is the phase and N is the number of cycles over which the averaging is performed.

Finally, the periodic fluctuations are denoted as:

$$\widehat{\chi}(\epsilon, y) = \widetilde{\chi}(\epsilon, y) - \overline{\chi}(y). \tag{10}$$

2.4. Details of numerical simulations

The open source in-house Xcompact3d framework (Laizet and Lamballais, 2009; Laizet and Li, 2011; Bartholomew et al., 2020) is used to perform numerical simulations. Sixth-order compact finite difference schemes are used for spatial discretization and a third-order explicit Runge–Kutta scheme is chosen for time integration. The condition of zero velocity divergence is ensured using a fractional step method, where a Poisson equation for the pressure gradient is solved with 3D FFTs (Laizet and Lamballais, 2009). For validation, two mesh resolutions, namely S_1 and S_2, are investigated and compared with reference simulations (see Table 1).

The first reference simulation (Abe et al., 2009) is utilized to validate the velocity statistics, while the second reference simulation (Seki et al., 2006) verifies the temperature statistics.

Mesh S_1 employs a fine spatial discretization but on a limited domain size. In contrast, Mesh S_2 encompasses a larger domain for the periodic directions, although with coarser grid resolution compared to Mesh S_1. Mesh S_1 exhibits approximately 1.5 times higher resolution in the wall-normal and spanwise directions and 2.15 times higher resolution in the streamwise direction.

In a previous study, using also the Xcompact3D code, it was demonstrated that increasing the numerical dissipation in the streamwise direction could, in certain cases, produce results equivalent to those obtained by increasing the spatial resolution (Flageul et al., 2015). This numerical dissipation is introduced using a fourth-order accurate spectral vanishing viscosity method (Lamballais et al., 2011). Consequently, additional dissipation is applied in the streamwise direction for the S_2 mesh only. Section 3 demonstrates that this configuration enables the S_2 mesh to yield results comparable to those obtained using the higher resolution S_1 grid, despite the reduced spatial resolution of S_2.

After a warm-up period of approximately 1500 (in t^+), stationarity was verified using the friction velocity and temperature.

3. Validation of uncontrolled numerical simulations

Figs. 2(a) and 2(b) represent the wall-normal distributions of the mean streamwise velocity and temperature, respectively. Simulations utilizing the S1 mesh are denoted by the solid blue lines, while the orange dashed lines indicate simulations on the S2 mesh. The black solid lines with crosses represent the reference data of Abe et al. (2009) providing the benchmark velocity profile and Seki et al. (2006)

Table 1
DNS unactuated computational conditions at $Re_\tau \approx 180$.

Cases	(Lx, Ly, Lz)	Δx^+	Δy^+_{min}	Δy^+_{max}	Δz^+	Δt^+	$T^+_{collect}$	Re_τ
Abe et al. (2009)	(12.8, 2, 6.4)	3.0	0.20	5.93	3.0	NA	3960	180
Seki et al. (2006)	(6.4, 2, 3.2)	1.1	0.05	0.97	1.1	NA	1677	180
S_1	(8, 2, 4)	4.96	0.29	4.13	3.53	$1.1\ 10^{-2}$	5613	178
S_2	(24, 2, 6)	10.68	0.43	6.16	5.34	$3.41\ 10^{-2}$	3790	179

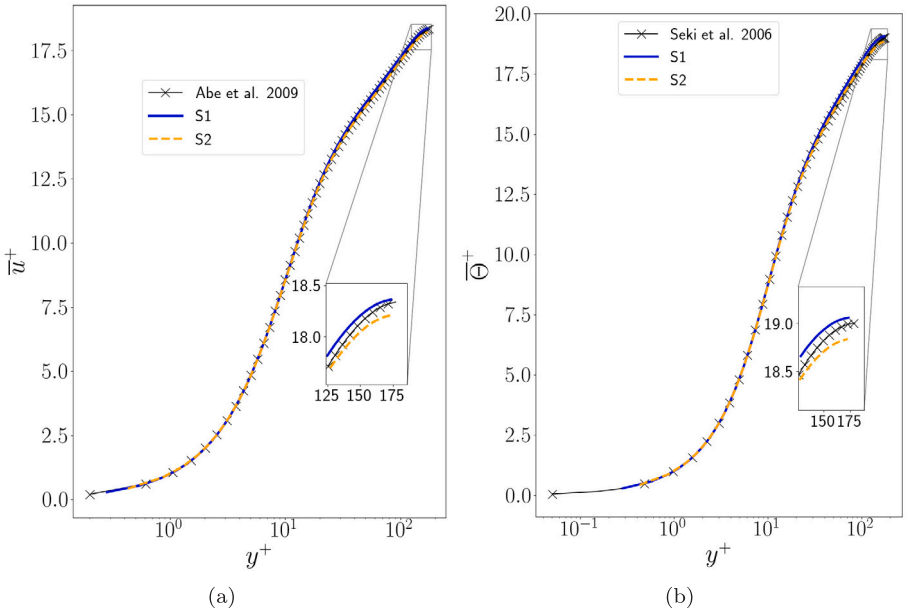

Fig. 2. Wall-normal distribution of the mean: (a) streamwise velocity and (b) temperature. Statistics obtained from simulations on S_1 and S_2 are represented by plain blue line and dashed orange line, respectively. Reference results (Abe et al., 2009; Seki et al., 2006) are shown by the black line with crosses.

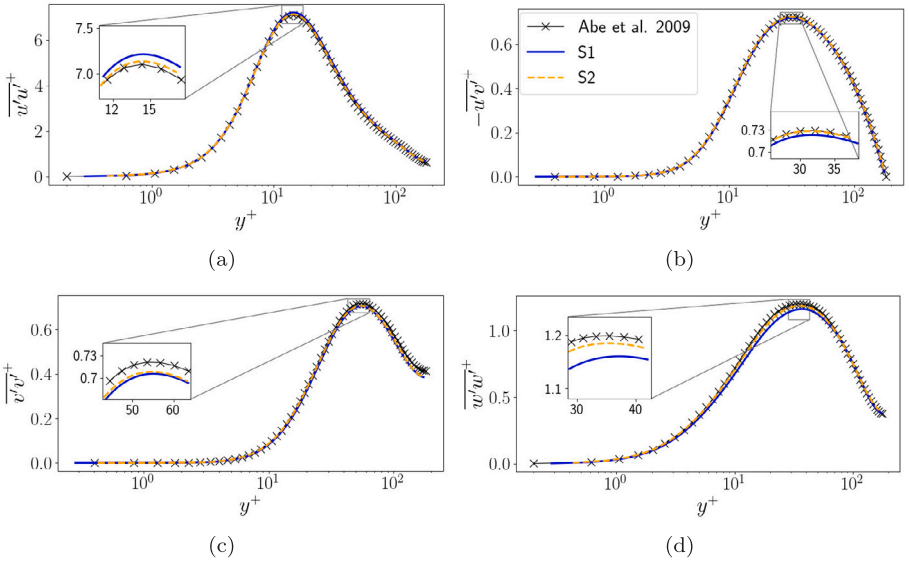

Fig. 3. Wall-normal distribution of the Reynolds stress components: (a) $\overline{u'u'}$, (b) $-\overline{u'v'}$, (c) $\overline{v'v'}$ and (d) $\overline{w'w'}$ in wall units. See caption of Fig. 2 for legend information.

supplying the temperature profile. For both variables, the current simulation results exhibit strong agreement with the reference data, with only negligible discrepancies in the channel centre that are statistically inconsequential.

Figs. 3 and 4 convey the second-order statistical moments for velocity and temperature, respectively. Fig. 3 shows the Reynolds stresses while Fig. 4 displays the temperature variance and turbulent heat fluxes. For the Reynolds stresses, both simulations exhibit excellent agreement with the reference data, with minor deviations mainly for the S_1 mesh. Specifically, the S_1 discretization slightly overpredicts the peak of $\overline{u'u'}$ (Fig. 3(a)) and underpredicts $\overline{w'w'}$ (Fig. 3(d)). The profiles of the wall shear stress $\overline{u'v'}$ (Fig. 3(b)) are nearly superimposed for both discretizations, indicating the accuracy of the prediction of this quantity.

Regarding temperature statistics in Fig. 4, unlike to the Reynolds stresses, the S_1 mesh results show marginally better agreement with

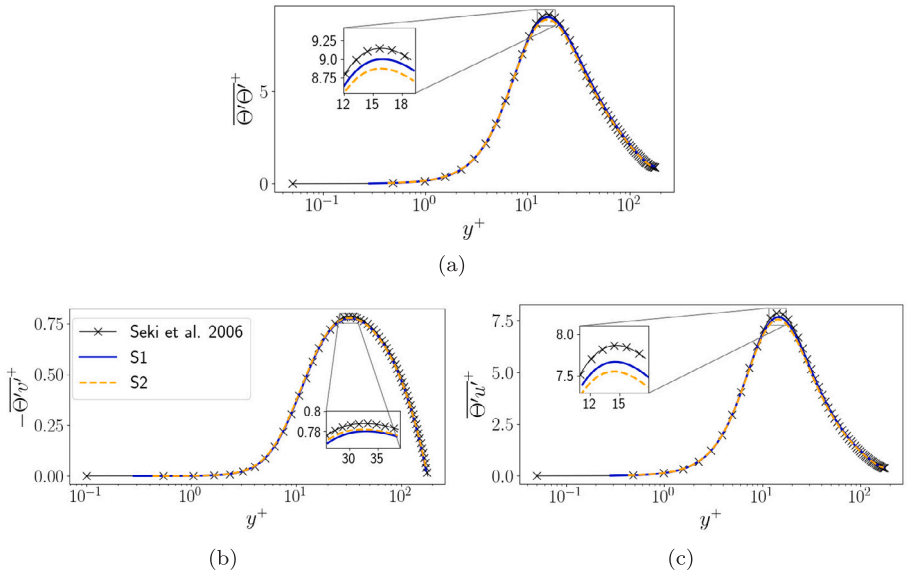

Fig. 4. Wall-normal distribution of the turbulent heat transport: (a) $\overline{\Theta'\Theta'}$, (b) $-\overline{\Theta'v'}$ and (c) $\overline{\Theta'u'}$ in wall units for Pr = 1. See caption of Fig. 2 for legend information.

Table 2
Mean friction coefficient and Nusselt number on mesh S_1 and S_2 against reference data.

Cases	$\langle C_f \rangle_t$	$\langle \mathrm{Nu} \rangle_t$
Abe et al. (2009)	$8.05\ 10^{-3}$	NA
Seki et al. (2006)	$8.43\ 10^{-3}$	21.07
Vreman and Kuerten (2014)	$8.11\ 10^{-3}$	NA
S_1	$8.05\ 10^{-3}$	20.65
S_2	$8.17\ 10^{-3}$	21.03

the reference data compared to the S_2 mesh. However, both simulations slightly underestimate the peaks of $\overline{u'\Theta'}$ and $\overline{\Theta'\Theta'}$. The discrepancy with the simulations of Seki et al. (2006) could result from their finer mesh resolution. However, their data were collected over a more limited spatial and temporal domain compared to the present study. This smaller sampling could cause statistics that are not fully converged. Overall, Figs. 3 and 4 highlight robust agreement with the reference statistics (Abe et al., 2009; Seki et al., 2006). Slight differences are likely attributable to statistical convergence.

Table 2 presents the temporal average of the friction coefficient $\langle C_f \rangle_t$ and Nusselt number $\langle \mathrm{Nu} \rangle_t$, which characterize drag and heat transfer, respectively. Comparison against three distinct sets of reference database serves to validate these quantities. Examining the S_2 mesh results, $\langle C_f \rangle_t$ lies between the reference values, with discrepancies of 3.2% with Seki et al. (2006), 1.4% against Abe et al. (2009), and 0.9% with Vreman and Kuerten (2014). The $\langle C_f \rangle_t$ value from the simulation on the S_1 mesh is equal to the one measured by Abe et al. (2009). Regarding the Nusselt number, the S_2 configuration exhibits a discrepancy of 0.2% with the results of Seki et al. (2006), while the S_1 configuration shows a larger deviation of 2.0%. Both discretizations accurately predict the relevant statistics in the present study, with the additional observation that the S_2 mesh demonstrates a lower error in computing the Nusselt number.

The pre-multiplied power spectral densities and the wall-normal distribution of the variance of the streamwise velocity and temperature are conveyed by Fig. 5. The left column shows spectra in the streamwise direction while the middle column shows spectra in the spanwise direction. The right column displays the wall-normal variation of $\overline{\chi'\chi'}$ obtained by integrating the pre-multiplied power spectral density $\Phi_{\chi'\chi'}$ along the wavelength:

$$\overline{\chi'\chi'} = \int_0^\infty \Phi_{\chi'\chi'} \mathrm{d}f = \int_0^\infty \lambda \Phi_{\chi'\chi'} \mathrm{d}\log\lambda. \tag{11}$$

These figures show the impact of the domain sizes of meshes S_1 and S_2. The isolines and second order stresses match closely between the two meshes, indicating that an increased resolution on S_2 would not necessarily improve the precision of results. This underpins the earlier hypothesis that the reference statistics from Seki et al. (2006) may not be fully converged. As expected, velocity spectrum peaks occur at $\lambda_x^+ \approx 1000$ and $\lambda_z^+ \approx 100$. The small S_1 domain size does not capture low-frequency content. See Tiselj (2014), Abe et al. (2004) for a deeper discussion on large scale structures and their impact on statistics.

Analysis of the streamwise velocity and temperature spectra reveals that the streamwise domain length of mesh S_2 is marginally adequate to capture the relevant flow physics. Quantitative assessment of the second-order statistics shows mesh S_2 provides slightly improved precision for predicting the turbulence quantities relevant for this study. Based on these assessments, mesh S_2 is selected for the remainder of this work, examining the effects of spanwise wall oscillations on variations in drag and convective heat transfer. The marginally enhanced domain size and sufficient resolution of S_2 are expected to provide more accurate quantification of the oscillation-induced changes in wall shear stress and Nusselt number under the actuation conditions considered.

4. Control strategy: Spanwise wall oscillations

4.1. Numerical simulation

The values of T, the control period, and W, the velocity amplitude, being fixed (see Fig. 1), the spanwise wall oscillations are enforced via the following time-dependent boundary condition:

$$w_\mathrm{w}(t_n) = W \sin(\frac{2\pi}{T} t_n) \tag{12}$$

where $t_n = n\Delta t$ denotes the discrete time at step index n, and Δt is the constant time step size of the numerical simulation. This formulation imposes an in-phase harmonic oscillation of the spanwise velocity w at the top and bottom walls.

To enable examination of the actuation effects, phase-averaged statistics are defined per Eqs. (8), (9) and (10). These leverage the inherent periodicity of the oscillatory forcing to delineate the statistical evolution across discrete phases within the actuation cycle. Such detailed interrogation is necessary to elucidate the fundamental physical phenomena governing the fluctuations in drag and heat transfer.

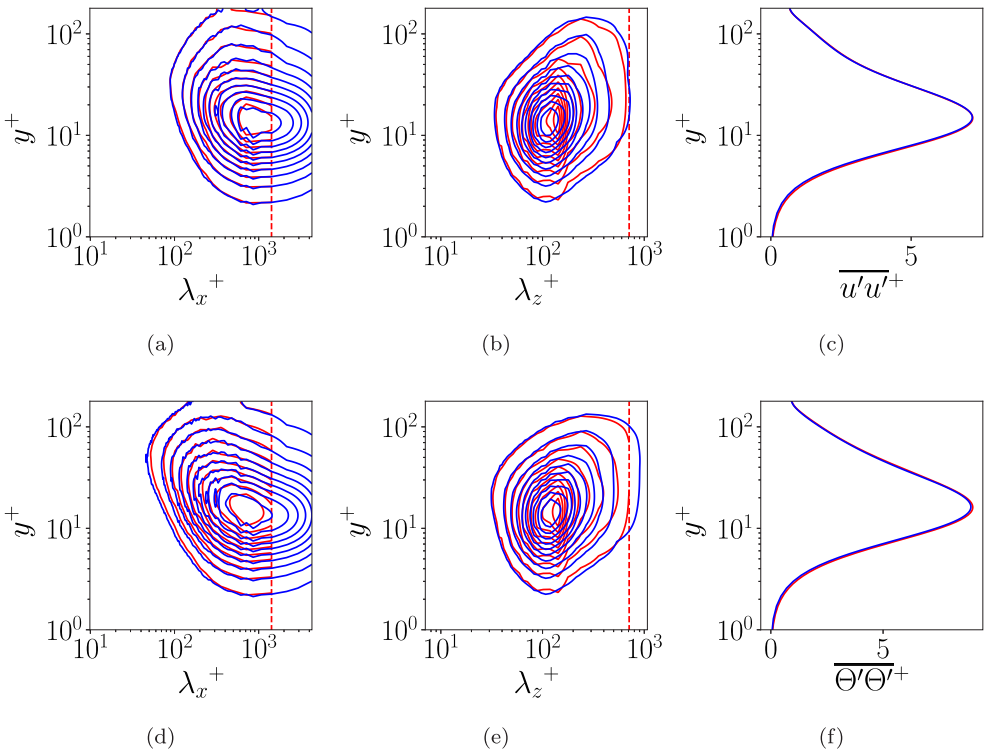

Fig. 5. (a, b): Pre-multiplied Power Spectral Densities of the streamwise velocity field $[k_\xi \Phi_{uu}(\lambda_\xi, y)]^+$: (a) in the streamwise direction, $\xi = x$, (b) in the spanwise direction, $\xi = z$, and (c) $\overline{u'u'}^+$ wall-normal distribution. (d,e,f): same quantities for the temperature field. Red isolines are the results obtained on mesh S_1 and blue isolines, on mesh S_2. Isoline levels span linearly between the minimal and maximal values. Red vertical dashed lines show the limit in domain size of mesh S_1. (For interpretation of the references to colour in this figure legend, the reader is referred to the web version of this article.)

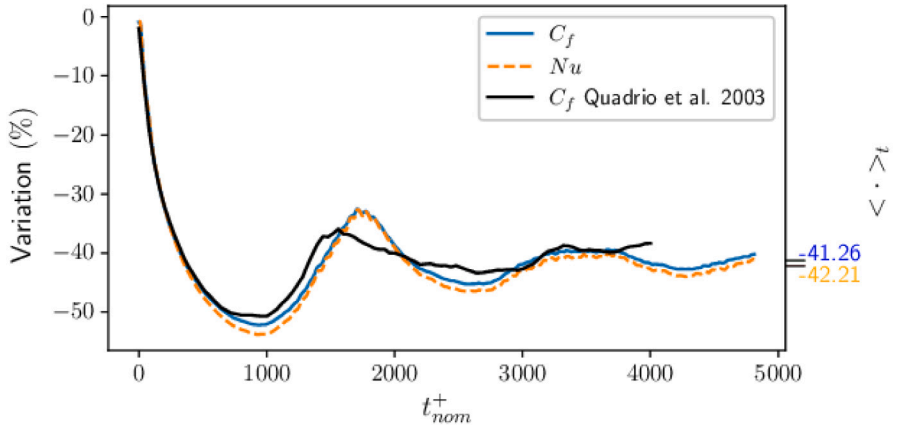

Fig. 6. Temporal evolution of drag and heat transfer reductions obtained by spanwise oscillatory wall actuation for control parameters $T^+_{\mathrm{nom}} = 125$ and $W^+_{\mathrm{nom}} = 18$. The black curve denotes data from Quadrio and Ricco (2003) for reference.

Due to the imposed oscillations and their periodic time-dependence, two variants of wall units may be employed for non-dimensionalization in the actuated flow:

- χ^+_{nom} where the normalization is based on the mean friction velocity for the unactuated flow ($\overline{u_{\tau,\mathrm{nom}}}$), the so-called nominal configuration;
- χ^+_{ac} where the mean friction velocity for the actuated flow ($\overline{u_{\tau,\mathrm{ac}}}$) is used for scaling.

For both computational meshes, the Courant–Friedrichs–Lewy (CFL) number was constrained under 0.5. Table 3 provides details on the actuated flow simulations performed in Section 5. To satisfy the CFL limit with Mesh S_2, the time step was reduced to compensate for CFL increase induced by the actuation (compare the values reported in Tables 1 and 3 for S_2). All fields were initialized using snapshots from the unactuated case taken in the statistically steady state. The warm-up period was set to 5 actuation cycles for the chosen set of oscillation parameters.

Table 3
Computational parameters of the actuated DNS for $T^+_{\mathrm{nom}} = 500$ and $W^+_{\mathrm{nom}} = 30$, values used in Section 5.

Cases	$\Delta t^+_{\mathrm{nom}}$	T^+_{collect}	number of cycles	phases per cycle: snapshots/stats
S_1	1.1 10^{-2}	11 500	23	32/288
S_2	1.56 10^{-2}	11 500	23	32/400

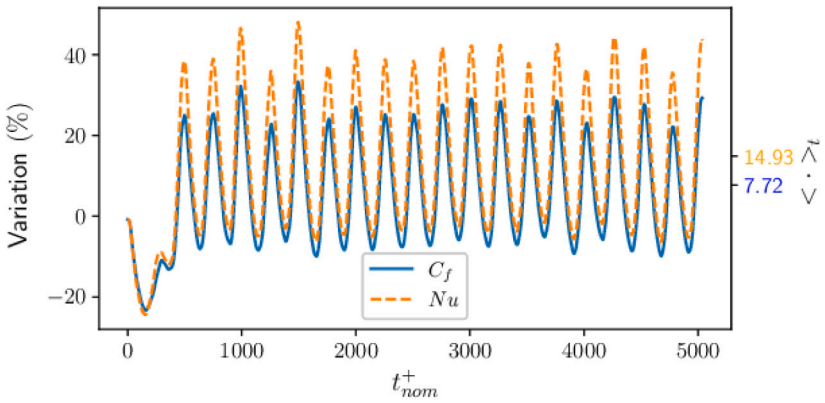

Fig. 7. Temporal evolution of drag and heat transfer augmentations obtained by spanwise oscillatory wall actuation for control parameters $T^+_{\mathrm{nom}} = 500$ and $W^+_{\mathrm{nom}} = 30$.

Relative to the unactuated case, attaining statistical convergence necessitates extended integration times, as precise representations are critical for each phase of the actuation cycle. Thirty-two snapshots were acquired evenly during each oscillation period, providing adequate resolution to compute power spectral densities and probability distribution functions across all actuation phases. The mesh utilized for the phase analysis of the first and second order moments is much more refined than the snapshot sampling. This furnishes the phase-resolved data essential for describing the physical processes governing the evolution of turbulence statistics, including drag and heat transfer, within each portion of the periodic actuation cycle.

Bradshaw and Pontikos (1985) were the first to recognize the crucial importance of the rate of change of the spanwise velocity gradient dW/dy, rather than the gradient itself, in reducing the intensity of near-wall turbulent structures and consequently the drag. They found that the spanwise shear needed to vary in space to sustain the drag reduction effect. However, it is important to note that the spanwise velocity gradient does not directly contribute to the drag experienced by the fluid moving along the channel. The spanwise gradient opposes the spanwise wall motion but does not hinder the fluid's streamwise motion. Numerous studies have conducted numerical simulations of turbulent channel flows subjected to spanwise wall oscillations while maintaining a constant streamwise pressure gradient (Quadrio and Ricco, 2004; Dong et al., 2019). Depending on the set of oscillation parameters, these simulations have demonstrated an increase in the flow rate, indicating a reduction in drag. This drag reduction occurs despite the presence of the spanwise velocity gradient, further emphasizing that the spanwise gradient does not directly participate in the overall drag experienced by the flow. Therefore, while the rate of change of the spanwise velocity gradient plays a crucial role in modulating the near-wall turbulence and consequently influencing the drag, it does not directly contribute to the drag itself. The drag reduction observed in numerical simulations with constant pressure gradient conditions underscores this point, as the flow rate increases despite the presence of the spanwise gradient. For these reasons, in the actuated case, the friction coefficient definition remains the same as stated in Eq. (5), based on the streamwise shear only.

4.2. Results for optimal drag reduction

Parametric studies at low Reynolds numbers have identified optimal dimensionless oscillation amplitude (W^+) and period (T^+) that maximize drag decrease. Significantly, Quadrio and Ricco (2003) demonstrated approximately 40% drag reduction (after the transient phase) at $\mathrm{Re}_\tau = 200$ utilizing control parameters equal to $W^+_{\mathrm{nom}} = 18$ and $T^+_{\mathrm{nom}} = 125$. In Fig. 6, the temporal evolution of the drag reduction obtained by Quadrio and Ricco (2003) is represented by the black line. The blue line depicts the analogous temporal drag variation at $Re_\tau = 180$, defined as:

$$\mathrm{Variation}(t) = \left(\frac{C_{f\,\mathrm{ac}}(t)}{\langle C_{f\,\mathrm{unac}} \rangle_t} - 1 \right) \times 100, \tag{13}$$

where the subscript "unac" refers to the uncontrolled configuration. The obtained trend closely resembles that of Quadrio and Ricco (2003), with the drag reduction converging to $\sim$ 40%, validating the implemented wall actuation methodology.

Additional code verification simulations were conducted using oscillation parameters of $T^+_{\mathrm{nom}} = 200$ and $W^+_{\mathrm{nom}} = 12$ on the $S2$ mesh. The resulting mean drag reduction (not shown here) exhibited a 2.10% deviation compared to the reference data of Quadrio and Ricco (2004). This minor deviation is statistically inconsequential and could potentially arise from lack of convergence or the documented Reynolds number effects described by Touber and Leschziner (2012). Specifically, they demonstrated that actuation efficacy diminishes with increasing Re_τ.

In Fig. 6, the temporal evolution of the Nusselt number is superimposed on the drag variation, revealing a strong correlation between the two quantities. The heat transfer reduction closely follows the drag reduction, with both reaching a decrease of approximately 40%. These findings emphasize the capability of spanwise wall oscillations to substantially reduce not only drag but also heat transfer. The tight coupling between the modulated heat transfer and drag aligns with previous observations by Fang and Lu (2010), who investigated active spanwise wall fluctuations in a compressible flow using LES. It is important to note, however, that their study employed a more complex form of wall motion, specifically out-of-phase and in-phase active spanwise wall fluctuations, which differs from the oscillatory forcing applied in the present work. Nonetheless, the qualitative agreement in the heat transfer and drag reduction trends underscores the robustness of the phenomenon across various flow regimes and actuation strategies.

5. Breaking the Reynolds analogy: Dissimilar enhancement of convective heat transfer

The disruption of near-wall streak formation by short-period oscillations has been demonstrated to reduce both drag and heat transfer, which aligns with expectations, as attenuated streaks diminish ejection and sweep events, thereby reducing mixing momentum. However, as oscillation periods increase, the potential for streak generation process can resume, which may intensify turbulent transport, leading to an increased drag and potentially heat transfer. This study investigates an actuation scenario that amplifies drag to characterize the associated

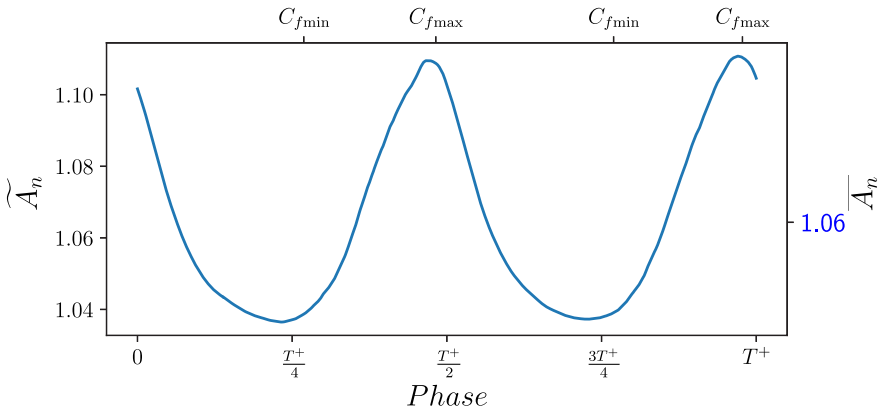

Fig. 8. Phase-wise averaged evolution of the analogy factor $\widetilde{A_n}$ obtained by spanwise oscillatory wall actuation for control parameters $T^+_{\text{nom}} = 500$ and $W^+_{\text{nom}} = 30$.

heat transfer response. To the authors' knowledge, as discussed in Section 1, the only reported case of drag amplification at low Reynolds numbers employed an oscillation period of $T^+_{\text{nom}} = 500$ (Jung et al., 1992). In contrast to the well-established drag-reduction case, where the decrease in drag is attributed to the reduced magnitude of streaks due to the interference of the Stokes layer with their formation process (Touber and Leschziner, 2012; Agostini et al., 2014a), the mechanisms driving the drag increase for $T^+_{\text{nom}} = 500$ remain unknown. Results demonstrating a strong coupling between drag and heat transfer responses for the drag-reducing scenario may not be directly extended to the drag-increase scenario. Therefore, before determining an optimal control scenario for enhancing heat transfer (which is beyond the scope of this paper), it is necessary to ascertain whether heat transfer increases concurrently with drag for $T^+_{\text{nom}} = 500$. If this is indeed the case, it is necessary to determine whether the Reynolds analogy holds or breaks down, with either drag or heat transfer being more significantly amplified.

5.1. Dissimilar heat transfer

Fig. 7 illustrates the temporal evolution of spatially-averaged drag and heat transfer under the influence of spanwise wall oscillations with control parameters $T^+_{\text{nom}} = 500$ and $W^+_{\text{nom}} = 30$. This amplitude value has been selected so that the Stokes layer penetrates the initial region of the buffer layer, where the streaks originate and develop. During the first half of the oscillation cycle, both heat transfer and skin friction experience a notable decrease of up to 25%. This initial reduction upon the onset of actuation aligns with previous findings and can be primarily attributed to the gradual penetration of the oscillatory Stokes layer into the viscous sublayer and buffer region, which disrupts the formation of streaks. Following this initial phase, the heat transfer and friction exhibit periodic oscillations at the actuation frequency corresponding to $T^+_{\text{nom}} = 500$. As observed in Agostini et al. (2014b), the effects on drag and heat transfer are consistent between the first and second halves of the cycle, despite rotating the streaks in opposite directions. The friction drag fluctuates between 5% below and 30% above the baseline, resulting in an average enhancement of 7.72%. In contrast, the heat transfer minima are slightly higher, while the maxima reach approximately 45% above the baseline. This disproportionate amplification of heat transport leads to an average thermal intensification of 14.93%, effectively doubling the increase in friction. These results emphasize the effectiveness of spanwise wall oscillations in enhancing turbulent heat convection. Furthermore, they reveal a significant asymmetry between the modulated heat transfer and drag, with the heat transfer oscillations exhibiting considerably larger amplitudes and gains compared to the friction fluctuations.

An analogy factor A_n is introduced to quantify differences between heat transfer and drag responses, as previously performed by Uchino et al. (2017). This factor, defined as the ratio of Nusselt number to friction coefficient for the actuated and unactuated configurations, is given by

$$A_n(t) = \frac{\text{Nu}_{\text{ac}}(t)/\overline{\text{Nu}_{\text{unac}}}}{C_{f\,\text{ac}}(t)/\overline{C_{f\,\text{unac}}}}. \tag{14}$$

Its phase and time averages can be deduced. They are given by

$$\widetilde{A_n} = \frac{\widetilde{\text{Nu}_{\text{ac}}}/\overline{\text{Nu}_{\text{unac}}}}{\widetilde{C_{f\,\text{ac}}}/\overline{C_{f\,\text{unac}}}}, \quad \text{and} \quad \overline{A_n} = \frac{\overline{\text{Nu}_{\text{ac}}}/\overline{\text{Nu}_{\text{unac}}}}{\overline{C_{f\,\text{ac}}}/\overline{C_{f\,\text{unac}}}}. \tag{15}$$

Control parameters resulting in $A_n > 1$ indicate greater heat-transfer enhancement relative to the drag increase.

Through the phase-averaged analogy factor $\widetilde{A_n}$, Fig. 8 distinctly shows the pronounced friction and heat-transfer asymmetry over oscillation phases. $\widetilde{A_n}$ reaches a minimum of slightly below 1.04 during friction minima. Meanwhile, it strengthens to 1.11 coinciding with peak friction coefficient. The shorter duration of $\widetilde{A_n}$ intensification compared to attenuation might indicate that distinct mechanisms drive the reduction and augmentation stages, and also lead to an average value of $\overline{A_n}$ equal to 1.06, highlighting a greater heat-transfer enhancement.

A comparison can be made to the streamwise travelling wave-like wall deformation used in Uchino et al. (2017) at $\text{Re}_\tau = 180$ with constant temperature difference (CTD) boundary conditions. They obtained an average analogy factor of $\overline{A_n} = 1.13$ with optimal parameters. Even though the control method is different, a comparison with the current study can be performed considering the similarities in Reynolds and Prandtl numbers. The current results using spanwise wall oscillations give a lower time-averaged value of $\overline{A_n} = 1.06$ with mixed boundary conditions. This reduced performance is likely because dissimilarity is more difficult to achieve using mixed versus CTD conditions, as shown in Kasagi et al. (2012). Additionally, only one parameter set was tested here, so higher analogy factors may be achievable by optimizing the parameters. Nevertheless, the mixed boundary conditions pose an inherent challenge for maximizing dissimilarity that steady CTD does not encounter, as stated in Section 1.

The first-order moments obtained for the actuated flow are compared to the unactuated case in Fig. 9. The black and green curves represent the total average values for the actuated and unactuated flows, respectively. In addition to these curves, the wall-normal distributions obtained for the phase-averaged values corresponding to $C_{f\max}$ and $C_{f\min}$ events are represented by the red and blue dotted lines, respectively. The wall-normal distributions of the time and phase averages of Θ and u are plotted in Figs. 9(a) and 9(b). A slight increase in $\overline{\Theta}$ is observed under the effect of the control, while no change is visible in the curves of $\overline{u}$. However, the curves showing the phase averages reveal that the actuation induces relatively moderate fluctuations, especially at the edge of the viscous sublayer.

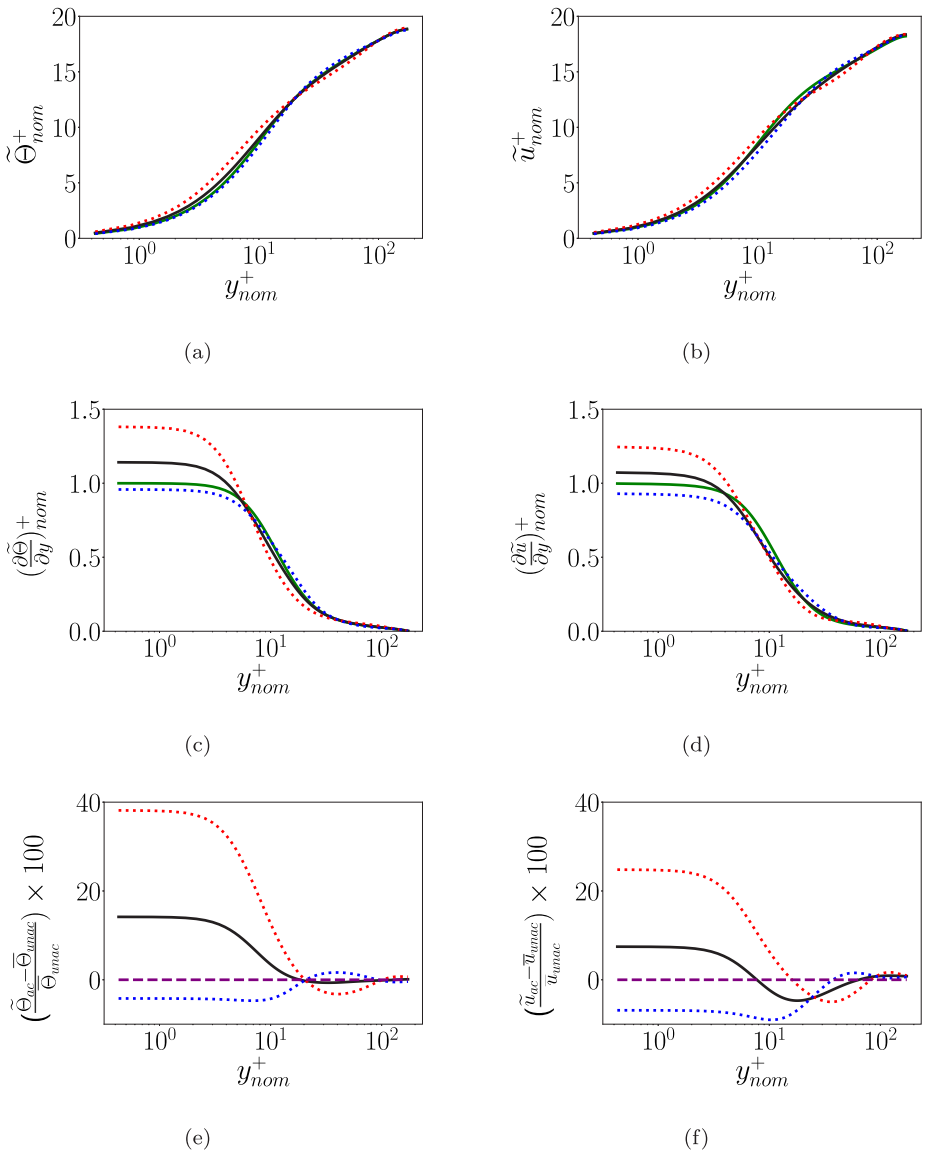

Fig. 9. Wall-normal distribution of the mean temperature (left column) and mean streamwise velocity (right column). (a, b): in nominal wall units, (c, d): derivative in the wall normal direction in nominal wall units, (e, f): variation with regards to the unactuated case (purple dashed lines indicate zero variation). Blue dotted lines indicate quantities at $C_{f\,\mathrm{min}}$ phases, red dotted lines during $C_{f\,\mathrm{max}}$ phases, black full lines the time averaged **actuated** case and green full lines the time averaged unactuated case. (For interpretation of the references to colour in this figure legend, the reader is referred to the web version of this article.)

To highlight the differences induced by the forcing, the wall-normal derivatives of Θ and u are shown in Figs. 9(c) and 9(d). These derivatives can be directly associated with the Nusselt and friction coefficients. The figures reveal that the actuation induces an increase for both variables, with a stronger effect on Θ compared to u. Furthermore, the phase variations are more significant for Θ, with the curve corresponding to $C_{f\,\mathrm{min}}$ being very close to the profile obtained for the unactuated case. This emphasizes that the actuation affects Θ more than u, leading to a slightly greater increase in Θ.

To quantify the increase, Figs. 9(e) and 9(f) show the relative increase in percentage compared to the unactuated flow. The results highlight that Θ is indeed more affected than u by the control, with stronger phase fluctuations. The curves for $C_{f\,\mathrm{min}}$ are slightly negative, but the value reached for $C_{f\,\mathrm{max}}$ events is almost twice as strong for Θ than for u, increasing by nearly 40%. The values obtained at the wall for the mean average show an increase of around 15% and 7.5% for Θ and u, respectively, in agreement with the results reported in Fig. 7. These figures shed light on the fact that the actuation affects Θ more than u, with a stronger amplification of Θ. Moreover, it can be highlighted from Figs. 9(c) and 9(d) that during $C_{f\,\mathrm{max}}$ events, the thermal sublayer thickness reduces slightly more significantly than the viscous sublayer's. The thickness of these sublayers can be represented by the extent of the plateau region at the wall. This observation concurs with more precise measurements comparing the reduction in the sublayer thicknesses from the unactuated to the actuated case at $C_{f\,\mathrm{max}}$ phases. Indeed, this comparison reveals a 26% decrease for the viscous sublayer against 31% for the thermal one.

The second-order statistics for Θ and u are investigated in Fig. 10, with their wall-normal distributions represented by dashed and solid lines, respectively. As in the previous figures, the values for the actuated and unactuated cases are represented by black and green lines, respectively. Fig. 10(a) shows that the variance for both variables strongly decreases when actuation is applied, with a slightly more significant weakening observed for Θ. These observations are quite surprising, as streamwise velocity fluctuations are typically associated with the magnitude of the streaks. The weakening of the variance suggests that the streaks are attenuated by the actuation, and thus, the drag increase is not directly related to the streak magnitude. It is also

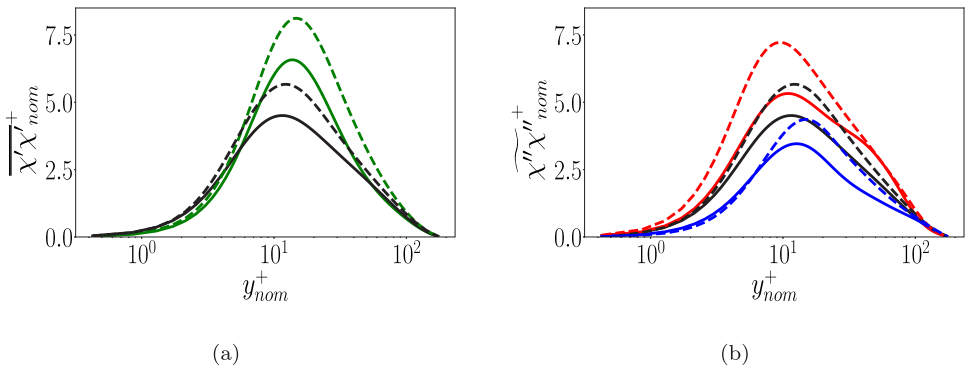

Fig. 10. Wall normal distributions of u and Θ variances, (solid): $\chi = u$, (dashed): $\chi = \Theta$. (a): unactuated against actuated, (b): all actuated cases. Black indicates quantities for the time averaged **actuated** case, green for the time averaged unactuated case, blue at $C_{f\,\mathrm{min}}$ phases and red during $C_{f\,\mathrm{max}}$ phases. (For interpretation of the references to colour in this figure legend, the reader is referred to the web version of this article.)

noteworthy that despite the Prandtl number being fixed at unity, the Θ fluctuations are stronger than those of u.

The phase-conditional wall-normal distributions of the variance are shown in Fig. 10(b), using the same colour code as previously used in Fig. 9. Several interesting observations can be made from these distributions. Firstly, as expected and in contrast to the previous observations, the maximum variance corresponds to the case where the drag is maximum. This suggests that the turbulent fluctuations are most energetic during the high-drag phase of the oscillation cycle. Furthermore, if the maximum value reached for each profile corresponds to the edge of the viscous or thermal sublayer, a more significant decrease in the thickness of the thermal sublayer can once more be observed during $C_{f\,\mathrm{max}}$ phases. This thinning of the thermal sublayer has important implications for the drag and heat transfer enhancement. The thickness of the sublayer is a crucial parameter to consider when examining the drag and heat transfer enhancement, as the mixing of momentum primarily occurs at the edge of the sublayer. If mixing takes place closer to the wall, its effect on the drag and heat transfer is expected to be substantial and drive their enhancement. To shed light on the magnitude of the mixing, structural changes of the streaks are first explored, as their rotation may induce stronger mixing. The cross-correlations between Θ and v, and between u and v, are then investigated in the following parts by measuring their contributions using the FIK identity and by analysing their joint probability density functions (PDFs).

The FIK identity, named after Fukagata, Iwamoto, and Kasagi (Fukagata et al., 2002), provides a framework for decomposing the friction coefficient and Nusselt number into contributions from different dynamical effects, such as the laminar, turbulent, and inhomogeneous terms. By evaluating the terms related to the Reynolds shear stresses $\overline{u'v'}$ and the turbulent heat flux $\overline{\Theta'v'}$, the relative importance of the momentum and thermal mixing can be quantified.

Moreover, the joint PDFs of u'-v' and Θ'-v' offer insights into the statistical structure of the turbulence and its phase-dependent behaviour. Previous studies have shown that drag-reducing actuation can lead to a narrowing of the joint PDFs and a reduction in the intensity of ejection and sweep events. Examining the joint PDFs at different phases of the oscillation cycle will reveal how the actuation modulates the turbulent mixing and its association with the drag and heat transfer enhancement.

5.2. Near-wall streak rotation and distortion under oscillatory conditions

In this section, the near-wall streaks' response to the spanwise oscillatory wall motion will be investigated. Structural changes will be discussed with a special focus set towards dissimilarities in between the temperature and momentum streaks.

Snapshots of the streamwise velocity and thermal fields, parallel to the wall and taken at the wall-normal locations corresponding to the peak of their variances, are presented in Figs. 11 and 12, respectively. The lower plots correspond to the first $C_{f\,\mathrm{min}}$ phase, while the upper plots correspond to the first $C_{f\,\mathrm{max}}$ phase. A few comments can be made.

- The imposed spanwise wall oscillations induce substantial structural modifications compared to canonical turbulent boundary layers, evident in the pronounced tilting and distortion of near-wall structures. The structures appear fundamentally distinct from the elongated high- and low-speed streaks inherent to unactuated turbulent flows.
- Fields corresponding to the $C_{f\,\mathrm{min}}$ phase show a strong tilting of the streaks, which is the most pronounced when compared to all other available phases. The streaks also appear more elongated. These observations are confirmed by performing a 2D correlation map for u in the streamwise and spanwise directions as given by

$$R_u^{x,z}(d_x, d_z) = \frac{\langle u'(\boldsymbol{x},t)u'(\boldsymbol{x} + d_x\boldsymbol{e_x} + d_z\boldsymbol{e_z},t)\rangle_{t,x,z}}{\left[\langle u'^2(\boldsymbol{x},t)\rangle_{t,x,z}\right]^{\frac{1}{2}}\left[\langle u'^2(\boldsymbol{x} + d_x\boldsymbol{e_x} + d_z\boldsymbol{e_z},t)\rangle_{t,x,z}\right]^{\frac{1}{2}}}. \tag{16}$$

  Fig. 13(b) conveys the map, revealing a streak reorientation angle of 61.8°.
- During the $C_{f\,\mathrm{max}}$ phases, the structures exhibit a stronger magnitude and more complex patterns. Visual comparison between the fields obtained for $C_{f\,\mathrm{min}}$ and $C_{f\,\mathrm{max}}$ reveals that the weakest structures during the $C_{f\,\mathrm{max}}$ phases have a similar tilting angle to those in the $C_{f\,\mathrm{min}}$ phases. However, the strongest structures are reoriented in the flow direction, with a tilting angle that appears to be half as large.
- The 2D correlation map presented in Fig. 13(a) confirms this observation. The isolines of correlation around the maximum value are oriented at an angle of 36.7° (see yellow line), while the isolines describing the tails of the correlation map show a stronger tilting at an angle of 51.8° (see purple line), closer to that observed at $C_{f\,\mathrm{min}}$ (blue line). The actuated 2D correlation map in Fig. 13(c) illustrates a reorientation angle very close to that corresponding to the $C_{f\,\mathrm{min}}$ phases for all its structures.
- Observations on the temperature 2D correlation maps (not shown here) lead to results analogous to the streamwise velocity. However, the tilting angle is approximately 3° higher for all cases except for the strongest structures at $C_{f\,\mathrm{max}}$ phases, where it is around 6° higher. This difference highlights the non-analogous distortion of the streaks in the velocity and temperature fields.

This analysis underscores the actuation-induced tilting of the streaks. Intriguingly, the strongest structures during the maximum friction phases are characterized by a lower angle of rotation. Although the temperature and velocity fields react to the actuation in a similar

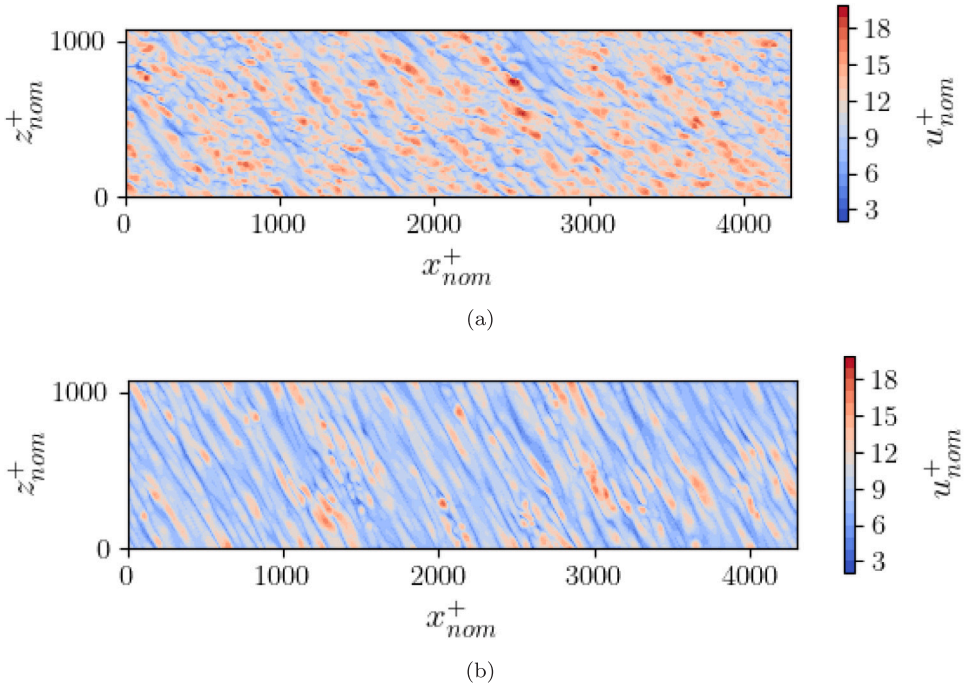

Fig. 11. Streamwise velocity field at $y^+_{\text{nom}} \approx 11.5$ in the actuated case with $T^+_{\text{nom}} = 500$ and $W^+_{\text{nom}} = 30$, at the phase corresponding to: (a) first $C_{f\,\text{max}}$ and (b) first $C_{f\,\text{min}}$ event.

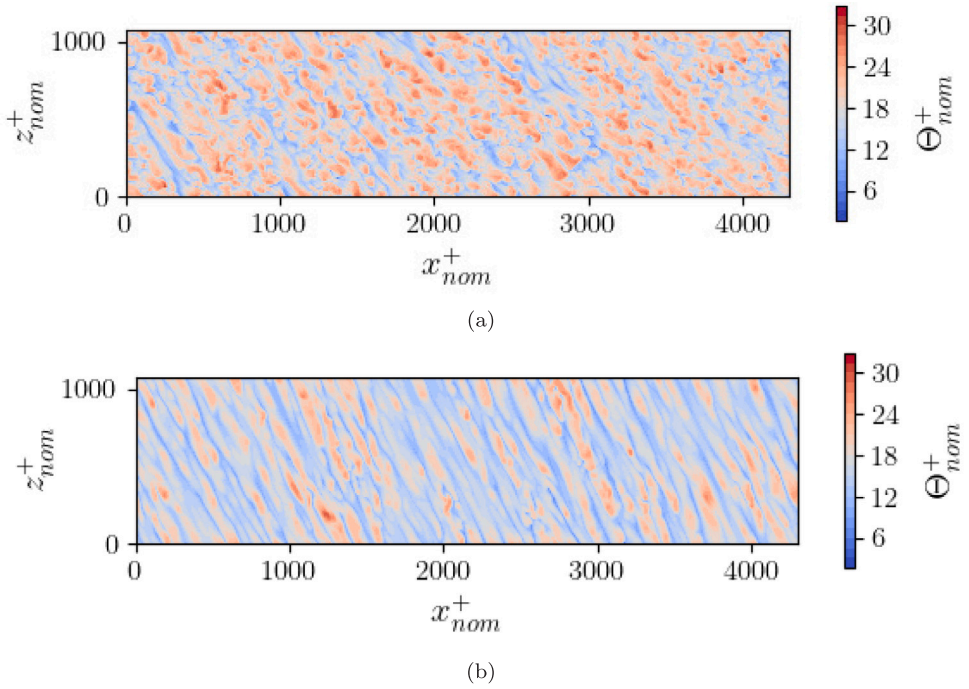

Fig. 12. Temperature field at $y^+_{\text{nom}} \approx 13.5$ in the actuated case with $T^+_{\text{nom}} = 500$ and $W^+_{\text{nom}} = 30$, at the phase corresponding to: (a) first $C_{f\,\text{max}}$ and (b) first $C_{f\,\text{min}}$ event.

manner, differences in their streak distortion are evident, which is consistent with the observed analogy breaking.

5.3. FIK identity component analysis of transport phenomena

This section aims to gain some insights on the mechanisms leading to the breakdown of the Reynolds analogy under imposed spanwise wall oscillations. To achieve this, the influence of the forcing terms appearing in the governing equations will be scrutinized. A secondary objective is to gain a more profound understanding of the connection between frictional quantities and turbulent stresses. In pursuit of these goals, a comprehensive decomposition of the friction coefficient and Nusselt/Stanton numbers into their constituent components will be performed by employing the FIK identities, as described in Gomez et al. (2009), and their thermal counterpart introduced in Hasegawa and Kasagi (2011).

The friction coefficient $\widetilde{C_f}$ is known to be directly linked to the turbulent shear stress $\widetilde{u''v''}$, while the Nusselt number is connected to the turbulent heat flux $\widetilde{\Theta''v''}$. This link will be investigated in the case of the actuated case using the FIK analysis, where it is expected

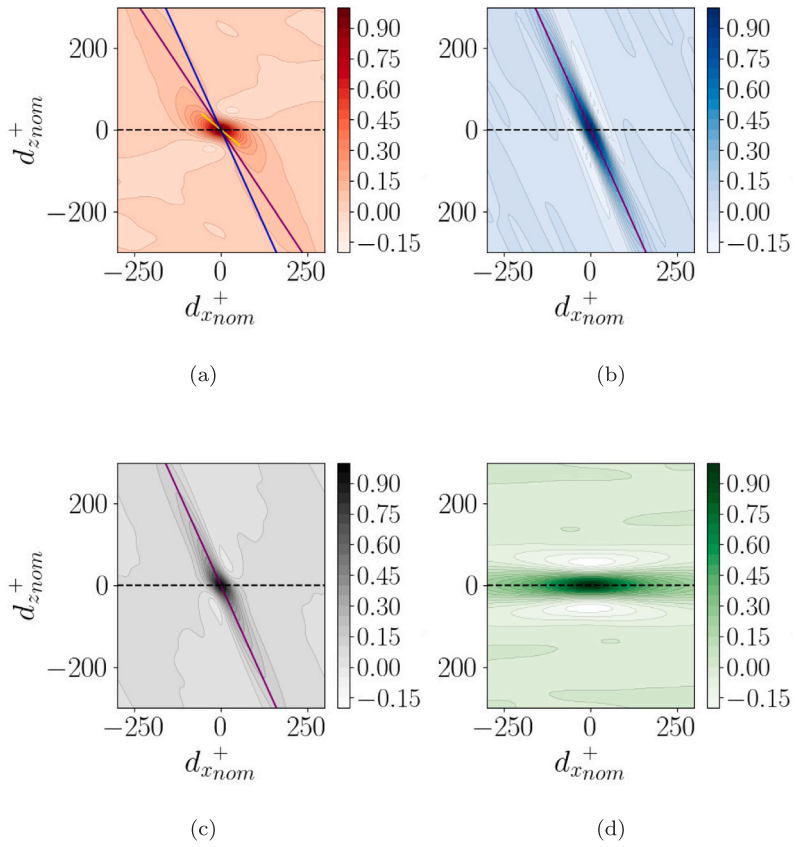

Fig. 13. 2D correlation maps of the streamwise velocity $R^{x,z+}_{u\,\mathrm{nom}}(d_x, d_z)$ at $y^+_{\mathrm{nom}} \approx 11.5$, in the actuated case with $T^+_{\mathrm{nom}} = 500$ and $W^+_{\mathrm{nom}} = 30$, at (a): $C_{f\,\mathrm{max}}$ phases, (b): $C_{f\,\mathrm{min}}$ phases, (c): **all phases**, and (d): the unactuated case. The purple line links the maximums of the tail of the correlation, while the yellow line does it for the strongest structures at the centre. The blue line replicates the purple line from (b). (For interpretation of the references to colour in this figure legend, the reader is referred to the web version of this article.)

that the more pronounced enhancement in heat transfer should also be discernible when comparing the turbulent shear stress and heat flux.

Adapting the FIK identities to the current configuration reveals the decompositions obtained for the Nusselt number and the friction coefficient averaged in time and phase, as detailed in the following equations:

$$
\begin{aligned}
\overline{\mathrm{Nu}} &= \underbrace{6}_{\mathrm{Nu_l}} + \underbrace{3\mathrm{Pe}\int_0^2 (y-1)\overline{\Theta'' v''}\,\mathrm{d}y}_{\mathrm{Nu_t}} - \underbrace{\frac{3\mathrm{Pe}A}{2}\int_0^2 (y-1)^2(\overline{u}_b - \overline{u})\,\mathrm{d}y}_{\mathrm{Nu_f}} \\
\widetilde{\mathrm{Nu}} &= \overline{\mathrm{Nu}} + \underbrace{3\mathrm{Pe}\int_0^2 (y-1)\widehat{\Theta'' v''}\,\mathrm{d}y}_{\mathrm{Nu_p}} \\
\overline{C_f} &= \underbrace{\frac{9}{\mathrm{Re}}}_{C_{f\mathrm{l}}} + \underbrace{\frac{27}{4}\int_0^2 (y-1)\overline{u'' v''}\,\mathrm{d}y}_{C_{f\mathrm{t}}} \\
\widetilde{C_f} &= \overline{C_f} + \underbrace{\frac{27}{4}\int_0^2 (y-1)\widehat{u'' v''}\,\mathrm{d}y}_{C_{f\mathrm{p}}}
\end{aligned}
\tag{5.2}
$$

The first constant component (C_{f_1} or $\mathrm{Nu_l}$) is referred to as the laminar component, the second (C_{f_t} or $\mathrm{Nu_t}$) represents the turbulent component, and the third (C_{f_p} or $\mathrm{Nu_p}$) is the periodic component. For the Nusselt number, the term $\mathrm{Nu_f}$ corresponds to the forcing term component, which is absent from the decomposition of the friction coefficient due to its negligible value. The turbulent and periodic components contain a weighting function $y-1$, which weights the shear stresses as a function of proximity to the wall. Consequently, shear stresses close to the wall contribute more significantly than those closer to the channel centre. Strategies that alter the magnitude or very near-wall distribution of turbulent shear stress and heat flux can therefore have a substantial impact on drag and heat transfer. For instance, a differential thinning of the thermal sublayer relative to the viscous sublayer could partially explain the observed dissimilarity in drag and heat transfer enhancement. Coincidentally, it was shown in Section 5.1 that the thinning of the thermal sublayer is more significant than the one of the viscous sublayer during maximum friction phases, where the dissimilarity is at its peak.

These formulations establish and clarify the direct link between drag/heat transfer and turbulent shear stress/heat flux while also distinguishing between turbulent components and their periodic fluctuations. Moreover, these decompositions elucidate the contribution of forcing terms to drag and heat transfer.

Fig. 14 shows the results derived from the FIK identity decomposition of the friction coefficient and Nusselt number under conditions of $T^+_{\mathrm{nom}} = 500$ and $W^+_{\mathrm{nom}} = 30$, relative to the unactuated scenario. Each component represented is normalized with respect to the total unactuated value. A notable distinction is observed in between each turbulent component where $\mathrm{Nu_t}$ shows more significant enhancement from which the dissimilarity arises. The greater positive periodic fluctuations highlights a more pronounced difference between the average and high intensity stresses, compared with the difference in between the low intensity and average values. This observed gap is far more pronounced for $\mathrm{Nu_p}$ than it is for C_{f_p}, highlighting once more how the

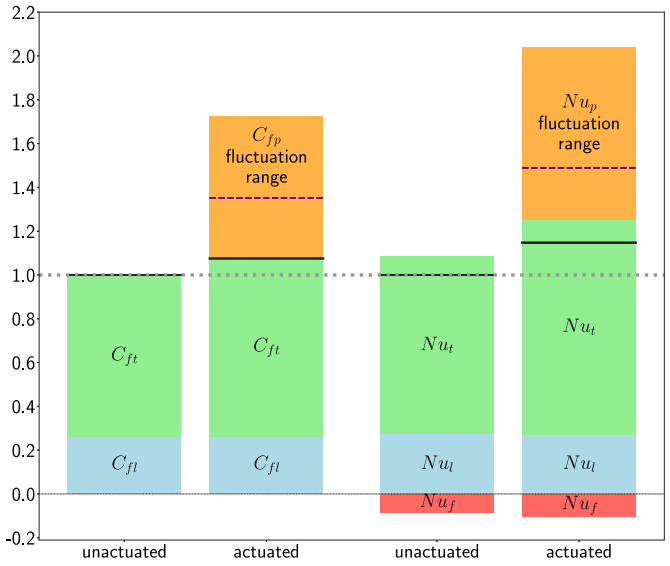

Fig. 14. FIK identity contributions of $\overline{C_f}/\overline{C_{f\,\mathrm{unac}}}$ and $\overline{\mathrm{Nu}}/\overline{\mathrm{Nu}_{\mathrm{unac}}}$. The actuated case corresponds to parameters $T^+ = 500$, $W^+ = 30$. Blue bins correspond to the laminar component, green bins to the turbulent component, red bins to the forcing term component and orange bins to the range of fluctuations of the periodic component. ..... : total unactuated value, ——— : total value, - - - : separation of negative and positive fluctuations. (For interpretation of the references to colour in this figure legend, the reader is referred to the web version of this article.)

phases of maximum friction carry the highest dissimilarity. Negative values of the $\mathrm{Nu_f}$ component weaken heat transfer, as shown by the red bins. However, the small differences between actuated and unactuated $\mathrm{Nu_f}$ suggest that the forcing term has a negligible effect on increasing heat transfer, therefore on the dissimilarity. Given the insignificance of the forcing term, the only two remaining possible causes of dissimilarity are the solenoidal velocity condition (applied by the pressure term in the streamwise velocity equation) or the linear temperature equation (see Section 2).

Fig. 15 shows the wall-normal distribution of the weighted actuated turbulent shear stress and heat flux based on the FIK identity turbulent components. The red lines correspond to the maximum drag phases, the blue lines to the minimum drag phases and the black lines represent the time average, while the green lines, for reference, show the time-averaged distributions obtained for the unactuated case.

From Fig. 15(a), it is clear that the increase in drag is due to the actuation-induced increase in the weighted turbulent shear stress near the wall, which extends to the peak. This influence on drag is particularly pronounced, given the weight function in the turbulent terms of the FIK identities. A similar conclusion can be drawn for the turbulent heat flux, albeit with a more substantial increase in the weighted stress around the peak, characterizing the stronger heat transfer enhancement. As visible in Fig. 15(b), during minimum friction phases, this gap starts further away from the wall, implying lower dissimilarity. During maximum friction phases, the stronger enhancement of the heat flux relative to the shear stress starts closer to the wall and is more significant, as expected.

Indeed, the dissimilarity in between the increases in drag and heat transfer becomes more apparent when examining the profiles of turbulent shear stress and heat flux, which results in the enhancement in heat transfer exceeding that of drag, leading to the observed dissimilarity with $\overline{A_n} = 1.06$. A detailed comparison between the $C_{f\,\mathrm{min}}$ and $C_{f\,\mathrm{max}}$ phases has shown the importance of the weighted stresses' influence on the dissimilarity. In addition, this analysis reaffirms the observation that phases marked by pronounced fluctuations in velocity and temperature are further away from time-averaged quantities, even more so for temperature.

5.4. Actuation induced enhancement of momentum and thermal mixing

In the previous section, it was demonstrated how the increase in near wall turbulent shear stress and heat flux results in better mixing, implying drag and heat transfer enhancement. In this section, it is attempted to obtain a deeper understanding of the mixing enhancement through quadrant analysis.

Fig. 16 highlights the probability density functions of the wall normal velocity fluctuations joint with the streamwise velocity/temperature fluctuations. They are weighted by the absolute values of the fluctuations product in order to separate each quadrants. The dominant quadrants for these quantities are the ejection and sweeps, as is shown in the unactuated case. Comparing the actuated to the unactuated case highlights a pronounced enhancement of the wall normal velocity fluctuations, which is strongest during $C_{f\,\mathrm{max}}$ phases and weakest during $C_{f\,\mathrm{min}}$ phases. The $C_{f\,\mathrm{max}}$ phases also show more enhanced ejections when comparing with the $C_{f\,\mathrm{min}}$ phases, balancing the outer layer sweeps. The magnitude of the temperature/streamwise velocity streaks was previously shown to reduce with the oscillation (see Fig. 10), even during $C_{f\,\mathrm{max}}$ phases. This is a major difference when comparing with the drag reduction mechanism where the decrease of the structure's intensity plays a substantial part. Therefore, this decrease is compensated by a better mixing in between the near wall and outer layers, highlighted by the enhanced sweep and ejection events in the wall normal direction. This improvement of momentum/thermal

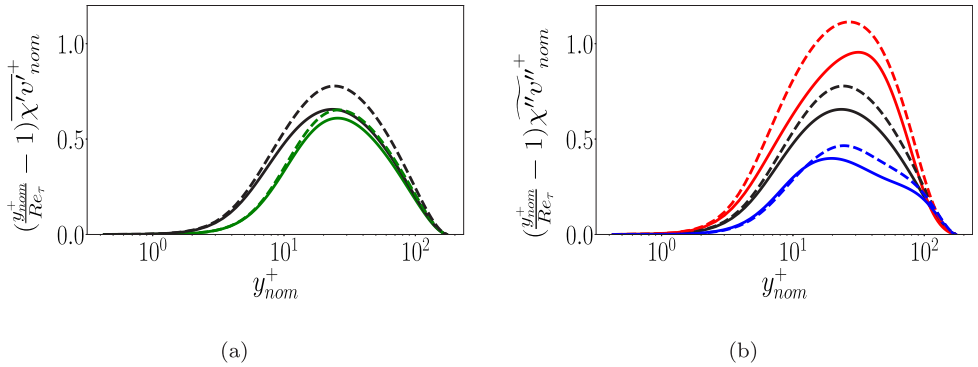

Fig. 15. Wall normal distributions of weighted turbulent shear stress and heat flux, (solid): $\chi = u$, (dashed): $\chi = \Theta$. (a): unactuated against actuated, (b): all actuated cases. Blue indicates quantities at $C_{f\,\mathrm{min}}$ phases, red during $C_{f\,\mathrm{max}}$ phases, black the time averaged **actuated** case and green the time averaged unactuated case. (For interpretation of the references to colour in this figure legend, the reader is referred to the web version of this article.)

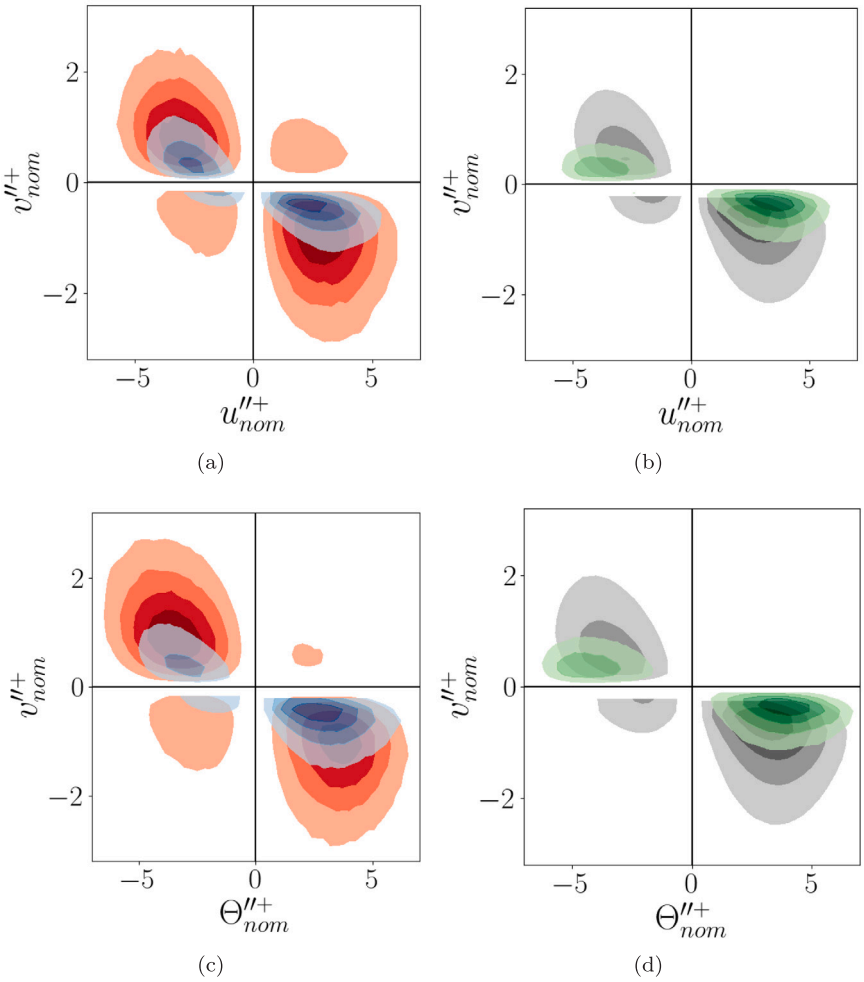

Fig. 16. Normalized quadrant-conditioned joint PDF (a,b): $|u''v''|\ P(u'',v'')$ at $y^{+}_{\mathrm{nom}} = 11.5$, (c,d): $|\Theta''v''|\ P(\Theta'',v'')$ at $y^{+}_{\mathrm{nom}} = 13.5$. Blue indicates quantities at $C_{f\,\mathrm{min}}$ phases, red during $C_{f\,\mathrm{max}}$ phases, black the **actuated** case and green the unactuated case. (For interpretation of the references to colour in this figure legend, the reader is referred to the web version of this article.)

mixing results in the observed drag/heat transfer increases. Unfortunately, the probability density functions do not highlight any significant signs of dissimilarity.

6. Perspectives on mechanisms and correlations driving the Reynolds-analogy breakdown

The present study highlights notable differences in the mechanisms driving the breakdown of the Reynolds analogy compared to previous research on Kelvin–Helmholtz (K–H) rollers by Rouhi et al. (2022), Kuwata (2022). Unlike K–H rollers, spanwise-wall motion fails to generate strong vortical motion that creates separation regions, which typically decrease drag while increasing heat transfer. This study finds that the breakdown occurs only when drag is increased, suggesting that different mechanisms may be at play. However, analysis of velocity correlations reveals a stronger correlation between v and Θ than between v and u, indicating that sweep and ejection motions have a more significant impact on heat transfer than on drag. This effect is amplified when drag reaches its maximum, resulting in a 40% increase in heat transfer compared to a 20% increase in drag. These results suggest that the mechanism driving the breakdown of the Reynolds analogy in this study might share some similarities with those observed in K–H rollers. Given the contrasting indications from these observations, it remains unclear whether the mechanisms at play are entirely different from or share similarities with those observed with K–H rollers. Further investigation is required to clarify this ambiguity.

Furthermore, the pressure–velocity correlation term appears to weaken Reynolds stresses while having minimal impact on the v-Θ correlation. This allows the v-Θ term to remain efficient and dominate the heat transfer process, potentially explaining the breakdown of the Reynolds analogy in this case. The dichotomy between the effects on drag and heat transfer may be a key factor in the observed phenomenon. To gain a deeper understanding of the mechanisms involved, further research is essential. Future studies should focus on exploring the hypothesis surrounding the role of the pressure–velocity correlation term, shedding light on the underlying mechanisms, and investigating potential similarities and differences with the mechanisms observed in K–H rollers.

7. Conclusion

The efficacy of spanwise wall oscillations as a versatile technique for manipulating both drag and heat transfer in turbulent channel flow is elucidated by the present study. Through direct numerical simulations conducted at $\mathrm{Re}_\tau = 180$ and $\mathrm{Pr} = 1$, it is demonstrated that:

– Heat transfer can be attenuated by employing oscillation parameters known to reduce drag, such as $T^+ = 125$ and $W^+ = 18$. Under these conditions, the reduction in heat transfer and drag go hand in hand, thus preserving the Reynolds analogy. This behaviour is anticipated, as these control parameters suppress streak formation

and the associated ejection-sweep motions, thereby weakening the turbulent mixing that governs both momentum and heat transport.
- In contrast, the results demonstrate that heat transfer can be enhanced by increasing the oscillation period. By setting $T^+ = 500$ and $W^+ = 30$, a substantial enhancement in heat transfer is observed, underscoring the potential of spanwise wall oscillations as a mean to intensify thermal transport.
- Remarkably, under the extended oscillation period and amplitude, the heat transfer intensification of 15% markedly surpasses the modest 7% drag increase. This dissimilarity between heat transfer and drag points to a breakdown of the Reynolds analogy, highlighting the potential of spanwise wall oscillations for optimizing heat exchanger performance.
- The oscillations induce a spanwise tilting of the streaks which is most significant during $C_{f\,\mathrm{min}}$ phases and not as important for the strongest structures during the $C_{f\,\mathrm{max}}$ phases. Furthermore, this rotation is shown to be slightly superior for the temperature streaks, which aligns with the analogy breaking.
- The FIK identity analysis shed light on the physical mechanisms governing the observed heat transfer enhancement exceeding drag rise under spanwise wall oscillations. The negligible impact of the forcing terms showed, by elimination, that the perceived dissimilarity arises from the pressure term in the streamwise velocity equation and the linearity of the temperature equation. To strengthen the dissimilarity, the turbulent heat flux has to be amplified over the turbulent shear stress in the near wall region, which was achieved in the present work.
- The current study provides compelling evidence that mixing momentum associated with sweep/ejection events is amplified for the actuated case, despite the apparent diminution of the streak amplitude. This enhanced mixing leads to a thinner thermal sublayer in comparison to the viscous sublayer, during the maximum drag phases, where the dissimilarity is the highest. As a result, the intensification of heat transfer surpasses the drag increase, potentially influenced by the pressure redistribution term. However, further investigation is necessary to confirm this hypothesis. These results highlight the complexity of the interactions between the oscillatory Stokes layer and the turbulent flow structures, which extend beyond a simple dependence on streak strength. Further research is essential to elucidate the intricate mechanisms governing these interactions and their profound impact on thermal transport in actuated turbulent boundary layers.

The foundation for future research aimed at exploiting the dissimilarity between heat transfer and drag through spanwise wall oscillations is laid by the present work. By gaining a deeper understanding of the fundamental mechanisms driving this phenomenon, the development of optimized flow control strategies designed to enhance heat exchanger efficiency can be guided. Future studies should focus on systematically exploring the parameter space to identify the optimal oscillation conditions that maximize heat transfer augmentation while minimizing drag penalties. This knowledge will be instrumental in designing the next generation of high-performance, energy-efficient heat transfer systems for a wide range of engineering applications.

CRediT authorship contribution statement

Lou Guérin: Writing – original draft, Validation, Software, Methodology, Formal analysis, Data curation. **Cédric Flageul:** Writing – review & editing, Supervision, Software, Methodology, Conceptualization. **Laurent Cordier:** Writing – review & editing, Supervision, Conceptualization. **Stéphane Grieu:** Writing – review & editing, Supervision, Conceptualization. **Lionel Agostini:** Writing – original draft, Supervision, Funding acquisition, Formal analysis, Conceptualization.

Declaration of competing interest

The authors declare that they have no known competing financial interests or personal relationships that could have appeared to influence the work reported in this paper.

Data availability

Data will be made available on request.

Acknowledgements

We express our sincere gratitude to Michael Leschziner, emeritus professor at Imperial College London, for his invaluable insights and guidance, which proved to be instrumental throughout the course of this research.

This work was granted access to the HPC resources of TGCC/CINES under the allocations AD012A14284 and A0152A07624 made by GENCI.

This work pertains to the French government program “Investissements d’Avenir” (EUR INTREE, reference ANR-18-EURE-0010, and LABEX INTERACTIFS, reference ANR-11-LABX-0017-01).

Fundings

Our research activities are supported by the French Agence Nationale de la Recherche (ANR), France in the framework of the project ”Apprentissage automatique pour les récepteurs solaires à haute température – SOLAIRE” (ANR-21-CE50-0031).

References

Abdulbari, H.A., Zulkifli, R., Salleh, M.Z., Yusoff, M.Z., 2013. Skin-friction drag reduction using riblets, dimples, and oscillating wall. J. Mech. Eng. Sci. 4, 452–464.

Abe, H., Antonia, R.A., Kawamura, H., 2009. Correlation between small-scale velocity and scalar fluctuations in a turbulent channel flow. J. Fluid Mech. 627, 1–32. http://dx.doi.org/10.1017/S0022112008005569.

Abe, Hiroyuki, Kawamura, Hiroshi, Choi, Haecheon, 2004. Very large-scale structures and their effects on the wall shear-stress fluctuations in a turbulent channel flow up to Retau=640. J. Fluids Eng. (ISSN: 0098-2202) 126 (5), 835–843. http://dx.doi.org/10.1115/1.1789528.

Agostini, L., Touber, E., Leschziner, M.A., 2014a. Spanwise oscillatory wall motion in channel flow: Drag-reduction mechanisms inferred from DNS-predicted phase-wise property variations. J. Fluid Mech. 743, 606–635.

Agostini, L., Touber, E., Leschziner, M., 2014b. The turbulence vorticity as a window to the physics of friction-drag reduction by oscillatory wall motion. Int. J. Heat Fluid Flow 51, http://dx.doi.org/10.1016/j.ijheatfluidflow.2014.08.002.

Asidin, S., Kuntjoro, W., Salleh, M.Z., 2019. A review on flow control methods in turbine internal cooling. Appl. Sci. 9 (16), 3233.

Bartholomew, P., Deskos, G., Frantz, R.A.S., Schuch, F.N., Lamballais, E., Laizet, S., 2020. Xcompact3D: An open-source framework for solving turbulence problems on a Cartesian mesh. SoftwareX (ISSN: 2352-7110) 12, 100550. http://dx.doi.org/10.1016/j.softx.2020.100550, URL https://www.sciencedirect.com/science/article/pii/S2352711019303620.

Bradshaw, P., Pontikos, N.S., 1985. Measurements in the turbulent boundary layer on an ‘infinite’ swept wing. J. Fluid Mech. 159, 105–130. http://dx.doi.org/10.1017/S0022112085003123.

Choi, Kwing-So, Clayton, B.R., 2001. The mechanism of turbulent drag reduction with wall oscillation. Int. J. Heat Fluid Flow 22, 1–9.

Dong, Haijun, Zhang, Yong, Deng, Fei, Liu, Wei, 2019. The research on fluid properties with spanwise-wall oscillation by LES WALE model. In: 2019 IEEE 4th International Conference on Advanced Robotics and Mechatronics. ICARM, pp. 966–969, URL https://api.semanticscholar.org/CorpusID:202561600.

Fang, J., Lu, L., 2010. Large eddy simulation of compressible turbulent channel flow with active spanwise wall fluctuations. Modern Phys. Lett. B 24, 1457–1460. http://dx.doi.org/10.1142/S0217984910023864.

Fang, J., Lu, L., Shao, L., 2009. Large eddy simulation of compressible turbulent channel flow with spanwise wall oscillation. Sci. China G 52, 1233–1243. http://dx.doi.org/10.1007/s11433-009-0165-3.

Fang, J., Lu, L., Shao, L., 2010. Heat transport mechanisms of low Mach number turbulent channel flow with spanwise wall oscillation. Acta Mech. Sin. 26, 391–399. http://dx.doi.org/10.1007/s10409-010-0343-6.

Flageul, C., Benhamadouche, S., Lamballais, E., Laurence, D., 2015. DNS of turbulent channel flow with conjugate heat transfer: Effect of thermal boundary conditions on the second moments and budgets. Int. J. Heat Fluid Flow (ISSN: 0142-727X) 55, 34–44. http://dx.doi.org/10.1016/j.ijheatfluidflow.2015.07.009, URL https://www.sciencedirect.com/science/article/pii/S0142727X15000910. Special Issue devoted to the 10th Int. Symposium on Engineering Turbulence Modelling and Measurements, ETMM10, held in Marbella, Spain on September 17–19, 2014.

Fukagata, Koji, Iwamoto, Kaoru, Kasagi, Nobuhide, 2002. Contribution of Reynolds stress distribution to the skin friction in wall-bounded flows. Phys. Fluids (ISSN: 1070-6631) 14 (11), L73–L76. http://dx.doi.org/10.1063/1.1516779.

Gatti, D., Quadrio, M., 2013. Performance losses of drag-reducing spanwise forcing at moderate values of the Reynolds number. Phys. Fluids 25 (12).

Gomez, T., Flutet, V., Sagaut, P., 2009. Contribution of Reynolds stress distribution to the skin friction in compressible turbulent channel flows. Phys. Rev. E 79, 035301. http://dx.doi.org/10.1103/PhysRevE.79.035301, URL https://link.aps.org/doi/10.1103/PhysRevE.79.035301.

Hasegawa, Y., Kasagi, N., 2011. Dissimilar control of momentum and heat transfer in a fully developed turbulent channel flow. J. Fluid Mech. 683, 57–93. http://dx.doi.org/10.1017/jfm.2011.248.

Jung, W., Mangiavacchi, N., Akhavan, R., 1992. Suppression of turbulence in wall-bounded flows by high-frequency spanwise oscillations. Phys. Fluids A 4, http://dx.doi.org/10.1063/1.858381.

Kaithakkal, A., Kametani, Y., Hasegawa, Y., 2021. Dissimilar heat transfer enhancement in a fully developed laminar channel flow subjected to a traveling wave-like wall blowing and suction. Int. J. Heat Mass Transfer 164, 120485. http://dx.doi.org/10.1016/j.ijheatmasstransfer.2020.120485.

Kasagi, N., Hasegawa, Y., Fukagata, K., Iwamoto, K., 2012. Control of turbulent transport: Less friction and more heat transfer. J. Heat Transfer (ISSN: 0022-1481) 134 (3), 031009. http://dx.doi.org/10.1115/1.4005151.

Kasagi, N., Tomita, Y., Kuroda, A., 1992. Direct numerical simulation of passive scalar field in a turbulent channel flow. J. Heat Transfer (ISSN: 0022-1481) 114 (3), 598–606. http://dx.doi.org/10.1115/1.2911323.

Kuwata, Y., 2022. Dissimilar turbulent heat transfer enhancement by Kelvin–Helmholtz rollers over high-aspect-ratio longitudinal ribs. J. Fluid Mech. 952, A21. http://dx.doi.org/10.1017/jfm.2022.915.

Laizet, S., Lamballais, E., 2009. High-order compact schemes for incompressible flows: A simple and efficient method with quasi-spectral accuracy. J. Comput. Phys. (ISSN: 0021-9991) 228 (16), 5989–6015. http://dx.doi.org/10.1016/j.jcp.2009.05.010.

Laizet, S., Li, N., 2011. Incompact3d: A powerful tool to tackle turbulence problems with up to O(105) computational cores. Internat. J. Numer. Methods Fluids 67, 1735–1757. http://dx.doi.org/10.1002/fld.2480.

Lamballais, E., Fortuné, V., Laizet, S., 2011. Straightforward high-order numerical dissipation via the viscous term for direct and large eddy simulation. J. Comput. Phys. (ISSN: 0021-9991) 230 (9), 3270–3275. http://dx.doi.org/10.1016/j.jcp.2011.01.040, URL https://www.sciencedirect.com/science/article/pii/S0021999111000659.

Marusic, I., Chandran, D., Rouhi, A., Fu, M.K., Wine, D., Holloway, B., Chung, D., Smits, A.J., 2021. An energy-efficient pathway to turbulent drag reduction. Nature Commun. 12 (1), 5805.

Ni, W., Lu, L., Ribault, C. Le, Fang, J., 2016. Direct numerical simulation of supersonic turbulent boundary layer with spanwise wall oscillation. Energies (ISSN: 1996-1073) 9 (3), URL https://www.mdpi.com/1996-1073/9/3/154.

Quadrio, M., Ricco, P., 2003. Initial response of a turbulent channel flow to spanwise oscillation of the walls. J. Turbul. 4, 1–23.

Quadrio, M., Ricco, P., 2004. Critical assessment of turbulent drag reduction through spanwise wall oscillations. J. Fluid Mech. 521, 251–271. http://dx.doi.org/10.1017/S0022112004001855.

Ricco, P., Skote, M., Leschziner, M.A., 2021. A review of turbulent skin-friction drag reduction by near-wall transverse forcing. Prog. Aerosp. Sci. 123, 100713. http://dx.doi.org/10.1016/j.paerosci.2021.100713.

Rouhi, Amirreza, Endrikat, Sebastian, Modesti, Davide, Sandberg, Richard D., Oda, Takuo, Tanimoto, Koichi, Hutchins, Nicholas, Chung, Daniel, 2022. Riblet-generated flow mechanisms that lead to local breaking of Reynolds analogy. J. Fluid Mech. 951, A45. http://dx.doi.org/10.1017/jfm.2022.880.

Seki, Y., Iwamoto, K., Kawamura, H., 2006. Prandtl number effect on turbulence statistics through high spatial resolution DNS of turbulent heat transfer in a channel flow. Trans. Japan Soc. Mech. Eng. B 72, 2856–2861.

Tiselj, Iztok, 2014. Tracking of large-scale structures in turbulent channel with direct numerical simulation of low Prandtl number passive scalar. Phys. Fluids (ISSN: 1070-6631) 26 (12), 125111. http://dx.doi.org/10.1063/1.4905018.

Touber, E., Leschziner, M.A., 2012. Near-wall streak modification by spanwise oscillatory wall motion and drag-reduction mechanisms. J. Fluid Mech. 693, 150–200. http://dx.doi.org/10.1017/jfm.2011.507.

Uchino, K., Mamori, H., Fukagata, K., 2017. Heat transfer in fully developed turbulent channel flow with streamwise traveling wave-like wall deformation. J. Therm. Sci. Technol. 12 (1), JTST0003. http://dx.doi.org/10.1299/jtst.2017jtst0003.

Viotti, C., Quadrio, M., Luchini, P., 2014. Streamwise oscillation of spanwise velocity at the wall of a channel for turbulent drag reduction. Phys. Fluids 26 (10), 101504.

Vreman, A.W., Kuerten, J.G.M., 2014. Comparison of direct numerical simulation databases of turbulent channel flow at $Re_\tau = 180$. Phys. Fluids 26, 015102.

Yamamoto, A., Hasegawa, Y., Kasagi, N., 2013. Optimal control of dissimilar heat and momentum transfer in a fully developed turbulent channel flow. J. Fluid Mech. 733, 189–220. http://dx.doi.org/10.1017/jfm.2013.436.

Zhang, X., Li, T., Jiang, N., 2020. Flow control strategies for improving performance of turbomachinery: A review. Prog. Aerosp. Sci. 115, 100595.